Part IV
Neurology

Chapter 17
PET Quantification in Molecular Brain Imaging Taking into Account the Contribution of the Radiometabolite Entering the Brain

Masanori Ichise, Yasuyuki Kimura, Hitoshi Shimada, Makoto Higuchi, and Tetsuya Suhara

Abstract A good understanding of the in vivo pharmacokinetics of radioligands is important for accurate PET quantification in molecular brain imaging. For many reversibly binding radioligands for which there exists a brain region devoid of molecular target binding sites called "reference tissue," data analysis methods that do not require blood data including the standardized uptake value ratio of target-to-reference tissue at a "fixed time point" (SUVR) and reference tissue model to estimate binding potential (BP_{ND}) are commonly used, the latter being directly proportional to the binding site density (B_{avail}). Theoretically, BP_{ND} is the tissue ratio minus 1 at equilibrium. It is generally believed that radioligands should not ideally produce radiometabolites that can enter the brain because they might complicate accurate quantification of specific binding of the parent radioligand. However, the tissue ratio that contains the contribution of radiometabolite can also be theoretically a valid parameter that reflects the target binding site density. This article describes the validation of the tissue ratio concept using, as an example of our recent PET data analysis approach for a novel radioligand, ^{11}C-PBB3, to quantify pathological tau accumulations in the brain of Alzheimer's disease patients in which the SUVR and reference tissue model methods using the cerebellar cortex as the reference tissue were validated by the dual-input graphical analysis model that uses the plasma parent and radiometabolite activity as input functions in order to take into account the contribution of the radiometabolite entering the brain.

Keywords PET quantification • SUVR • Binding potential • Radiometabolites • Tau • ^{11}C-PBB3 • Alzheimer's disease

M. Ichise, MD, Ph.D. (✉) • Y. Kimura, MD, Ph.D. • H. Shimada, MD, Ph.D. • M. Higuchi, MD, Ph.D. • T. Suhara, MD, Ph.D.
Molecular Imaging Center, National Institute of Radiological Sciences, 4-9-1 Anagawa, Inage-ku, Chiba, Chiba 263-8555, Japan
e-mail: ichisem@nirs.go.jp

Y. Kuge et al. (eds.), *Perspectives on Nuclear Medicine for Molecular Diagnosis and Integrated Therapy*, DOI 10.1007/978-4-431-55894-1_17

17.1 Introduction

Molecular brain imaging with positron emission tomography (PET) using radiolabeled ligands (radioligands) that target neuroreceptors/transporters and neuropathological biomarker proteins such as amyloid β (Aβ) proteins and pathological tau proteins has many exciting clinical and research applications. The major advantage of PET imaging is that PET using suitable radioligands allows for the accurate quantification of the target binding site density. For accurate PET quantification, however, a good understanding of the in vivo pharmacokinetics of radioligands is important.

For many reversibly binding radioligands for which there exists a brain region devoid of molecular target binding sites called "reference tissue," data analysis methods that do not require blood data including the standardized uptake value ratio (SUVR) method and reference tissue models to estimate binding potential (BP_{ND}) are commonly used to quantify specific molecular target binding sites. The validity of these simple methods can be evaluated by detailed pharmacokinetic modeling of dynamically acquired PET data and radiometabolite corrected arterial plasma parent radioligand activity as an input function. In this respect, it is generally believed that radioligands should not ideally produce metabolites that can enter the brain because they might complicate accurate quantification of specific binding of the parent radioligand.

The purpose of this article is to show that PET quantification using the SUVR and reference tissue model methods can also be valid even when the metabolite contributes to the measured brain radioactivity. In the theory section, the concept of PET measured "brain tissue ratios" in the context of radiometabolites entering the brain will be explored first, and then our recent PET data analysis approach for a novel radioligand, ^{11}C-PBB3 (2-((1*E*,3*E*)-4-(6-((^{11}C-methylamino)pyridin-3-yl) buta-1,3-dienyl) benzo[*d*]thiazol-6-ol) [1], to quantify pathological tau accumulations in the brain of Alzheimer's disease (AD) [2] will be highlighted as an example in which the SUVR and reference tissue model methods were validated by the dual-input graphical analysis model [3] that takes into account the contribution of the radiometabolite entering the brain.

17.2 Materials and Methods

17.2.1 Theory

PET data in molecular brain imaging are commonly analyzed by applying kinetic compartment models, which assume a compartmental system and derive the target binding parameters that reflect the densities of target binding sites in brain regions of interest (ROIs) [4]. Brain regions containing target binding sites (target tissue) have at least three compartments (or two-tissue (2T) compartments) (Fig. 17.1a

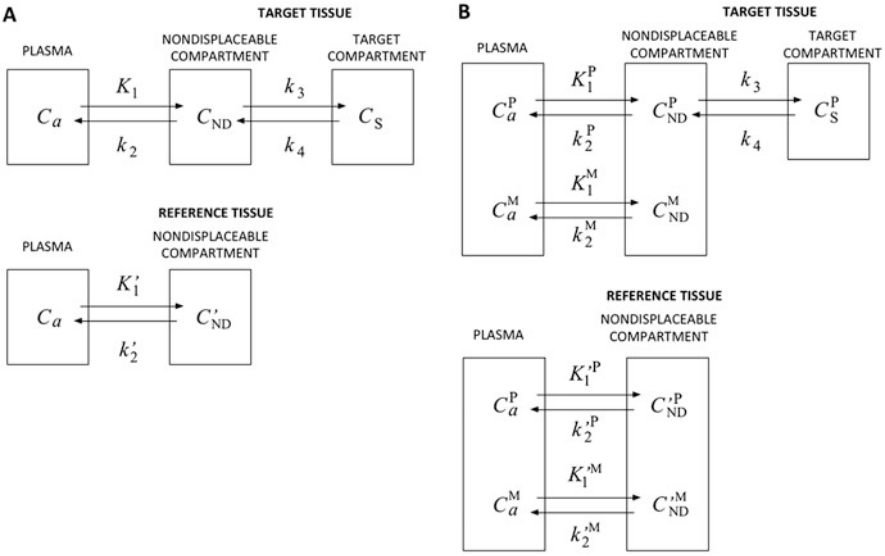

Fig. 17.1 Compartment configurations used to model in vivo radioligand kinetics when the parent only enters the brain (**a**) and both the parent and metabolite enter the brain (**b**). Terms are defined in the text

top). The first compartment is the arterial plasma (C_a), from which the unmetabolized parent radioligand passes into the second compartment or the first tissue compartment known as the nondisplaceable compartment (C_{ND}). The third compartment or the second tissue compartment (C_S) is the specific target binding sites. Reference tissue regions do not have the specific binding compartment (C_S) (Fig. 17.1a bottom). In Fig. 17.1a, K_1 (mL·mL^{-1}·min^{-1}) is the delivery rate constant; k_2 (min^{-1}), k_3 (min^{-1}), and k_4 (min^{-1}) are the first-order kinetic rate constants. Throughout the text, the prime sign is used to indicate the reference tissue. $C_B(t) = C_{ND}(t) + C_S(t)$ and $C_B'(t) = C_{ND}'(t)$ represent the target and reference tissue time activity, respectively, and $C_a(t)$ is the plasma parent radioligand activity at time t after the bolus radioligand administration.

Using $C_a(t)$ as an input function, compartment model approaches allow for the estimation of the distribution volume, V, which is the brain-to-plasma radioactivity ratio, $C_B(t)/C_a(t)$, at equilibrium in which there is no net transfer of radioligand activity between all compartments. Of note is that this equilibrium condition cannot be achieved in the PET experimental paradigm with a bolus radioligand administration. However, the compartment model analysis allows for the estimation of parameters defined at equilibrium. By assuming that the nondisplaceable distribution volume in the target tissue (V_{ND}) is the same as in the reference tissue (V_{ND}'), the target binding parameter, binding potential (BP_{ND}), is calculated as $V - V'/V' = V_S/V_{ND}$, which is directly proportional to the binding site density B_{avail}, i.e., $BP_{ND} = f_{ND}(B_{avail}/K_D)$, where f_{ND} and K_D represent the fraction of

nondisplaceable compartment from which the radioligand can exchange with the specifically bound compartment (free tissue fraction) and the equilibrium dissociation constant for radioligand-binding site complex, respectively [5]. The above relationship between BP_{ND} and B_{avail} is derived from the principle used in in vitro binding assays, which is in turn based on the bimolecular enzymatic reaction described by Michaelis and Menten [6]. Of note is that BP_{ND} can also be expressed as

$$BP_{ND} = \frac{V - V'}{V'} = \frac{\frac{C_B(t)}{C_a(t)} - \frac{C'_B(t)}{C_a(t)}}{\frac{C'_B(t)}{C_a(t)}} = \frac{C_B(t)}{C'_B(t)} - 1 \tag{17.1}$$

where t represents the time at which the compartment system is in equilibrium. BP_{ND} is, therefore, equivalent to the tissue ratio minus 1 at equilibrium.

Reference tissue models derived from the above compartment model estimate BP_{ND} by using $C'_B(t)$ as an input function without requiring arterial plasma data ($C_a(t)$) [4]. On the other hand, SUVR is the target-to-reference tissue ratio measured at a "fixed time point" after the bolus radioligand administration. The advantage of SUVR is that it can be calculated from static PET imaging data without the requirement of arterial data. SUVR $= C_B(t)/C'_B(t)$ is, therefore, closely related to BP_{ND} (Eq. 17.1), the differences between the two being that BP_{ND} is independent of radioligand delivery (blood flow) or its systemic clearance because it is defined at equilibrium,

On the other hand, in the situation where the metabolite enters the brain, the compartment system is more complex as shown in Fig. 17.1b in which superscripts P and M refer to "parent" and "metabolite," respectively, and the metabolite is assumed not to bind specifically to targets (see the discussion about the situation where the metabolite also binds specifically) [3]. Here, let's consider the tissue ratio minus 1 at equilibrium assuming that V_{ND} is the same in the reference and target tissues, which is given by

$$\begin{aligned} BP^*_{ND} &= \frac{C_B(t)}{C'_B(t)} - 1 = \frac{C^P_B(t) + C^M_B(t)}{C'^P_B(t) + C'^M_B(t)} - 1 = \frac{V^P + \delta V^M}{V'^P + \delta V'^M} - 1 \\ &= \frac{V_S}{V^P_{ND} + \delta V^M_{ND}} \end{aligned} \tag{17.2}$$

where δ is the metabolite-to-parent activity ratio in plasma at equilibrium $\left(\delta = C^M_a(t)/C^P_a(t)\right)$ and it is a constant value. This tissue ratio minus 1 at equilibrium has an additional term, δV^M_{ND}, the contribution of the metabolite nondisplaceable distribution volume in the denominator of Eq. 17.2, and it is here denoted by BP^*_{ND} to distinguish it from BP_{ND}, which is the tissue ratio minus 1 at equilibrium when only the parent enters the brain. To estimate this tissue ratio minus 1 by the reference tissue model, in fact, no knowledge of the metabolite

status is needed because it uses $C_B(t)$ as an input function. The same argument applies to the SUVR. Importantly, BP^*_{ND} like BP_{ND} is directly proportional to the target binding site density, B_{avail}, as shown below.

$$BP^*_{ND} = \frac{V_S}{V^P_{ND} + \delta V^M_{ND}} = \frac{f^P_P}{\frac{f^P_P}{f^P_{ND}} + \delta \frac{f^M_P}{f^M_{ND}}} \times \frac{B_{avail}}{K_D} \tag{17.3}$$

where f^P_P or f^M_P the free fraction of parent (P) or metabolite (M) in plasma is a constant and so are f^P_{ND}, f^M_{ND}, and δ in the same individual. Note that $V_S = f^P_P B_{avail}/K_D$ and V_{ND} can be expressed as f_P/f_{ND} because the free radioligand or metabolite activity in the plasma and the tissue compartments are the same at equilibrium $(f_P C_a(t) = f_{ND} C_{ND}(t))$ [4, 5]. The validation of the reference tissue model BP^*_{ND} can be accomplished by the dual-input graphical analysis model derived from the model illustrated by Fig. 17.1b that takes into account the contribution of radiometabolites entering the brain using the combined plasma radioactivity $\left(C^P_a(t) + C^M_a(t)\right)$ as an input function [3]. The operational equation is given by

$$\frac{\int_0^t C_B(t)dt}{C_B(t)} = \alpha(t) \frac{\int_0^t \left(C^P_a(t) + C^M_a(t)\right)\ dt}{C_B(t)} + \beta(t) \tag{17.4}$$

Eq. 17.4 becomes linear when the system reaches transient equilibrium between the brain and plasma compartments at time t^* and both the slope α and intercept β can be considered constant beyond t^*. The tissue ratio minus 1 at equilibrium is calculated as

$$BP^*_{ND} = \frac{V_S}{V^P_{ND} + \delta V^M_{ND}} = \frac{\alpha_{\text{target tissue}}}{\alpha_{reference\ \ \text{tissue}}} - 1.$$

The tissue ratio minus 1 at equilibrium can also be estimated by the traditional compartment model (Fig. 17.1a) using the parent-only input function ($C^P_a(t)$) if data fitting can be adequately accomplished. However, it may not match the tissue ratio minus 1 estimated by the reference tissue model or the dual-input model if a significant amount of the metabolite is entering the brain because the tissue radioactivity includes the metabolite contribution, which is not accounted for by the traditional compartment model (Fig. 17.1a).

17.2.2 Radioligand

^{11}C-PBB3 is a novel radioligand developed at the National Institute of Radiological Sciences, Chiba, Japan, for PET imaging of pathological tau aggregates in the brain [1]. Neurofibrillary tau tangles are one of the two pathological hallmarks of AD, the

other being the senile plaques containing Aβ deposition [7]. ^{11}C-PBB3 binds reversibly to neurofibrillary tau tangles of a wide range of isoform compositions with high affinity ($K_D = 2.5$ nM) and selectivity [1]. ^{11}C-PBB3 upon intravenous administration is rapidly converted in plasma to one major radiometabolite identical chemically in both humans and mice, a significant amount of which enters the mouse brain (30% of radioactivity in brain 5 min after injection) [8]. ^{11}C-PBB3 SUVR in AD patients has previously been shown to reflect the known pathological tau distribution at various stages of AD [9].

17.2.3 PET Data

The reader is referred to our recent ^{11}C-PBB3 PET data analysis study [2] regarding the detail of PET data acquisition and full data analysis. Here, the description is limited to information relevant to illustrating the concept of tissue ratio estimation considering the contribution of radiometabolite to the brain activity.

^{11}C-PBB3 PET data consisted of 70 min dynamic scans after a bolus injection of approximately 400 MBq of ^{11}C-PBB3 in 7 AD patients (76 ± 7 y) and 7 elderly healthy control subjects (70 ± 6 y). Input functions ($C_a^P(t)$ and $C_a^M(t)$) were obtained from multiple arterial samples by determining plasma fractions of the parent and its radiometabolites with high-performance liquid chromatography.

To improve the statistical quality of PET ROI data, we generated cerebral cortical ROIs pooling all voxels of high (>0.3, high), medium (0.15–0.3, middle), low (0–0.15, low), and non-binding (<0) BP^*_{ND} values on preliminarily generated parametric images by the original multilinear reference tissue model ($MRTM_O$)[10] using the cerebellar cortex as the reference tissue because tau accumulation is known to be histopathologically absent in the cerebellar cortex of either normal or AD brains [11].

17.2.4 Data Analysis

The tissue ratio minus 1 was estimated in four ways using cerebral cortical ROI data with the cerebellar cortex as the reference tissue:

1) BP^*_{ND} estimation by the dual-input graphical analysis using $\left(C_a^P(t) + C_a^M(t)\right)$ as an input function (Eq. 17.4)
2) BP_{ND} estimation by 2T compartment kinetic analysis using $C_a^P(t)$ as an input function (Fig. 17.1a)
3) BP^*_{ND} estimation by the reference tissue model $MRTM_O$ using $C'_B(t)$ as an input function
4) SUVR minus 1 at a fixed time point (50 min–70 min)

The tissue ratio minus 1 values obtained by the above 4 methods were then compared to validate the use of SUVR and the reference tissue model BP^*_{ND}. Additionally, parametric images of $MRTM_O$ and (SUVR-1) were generated and compared.

17.3 Results

The brain ^{11}C-PBB3 time activity curves (TACs) quickly peaked within a few minutes of intravenous injection of ^{11}C-PBB3 with gradual decreases thereafter with a significantly slower washout for high binding cerebral cortex in ADs than in HCs (Fig. 17.2a). Plasma parent TACs peaked very quickly and decreased also quickly thereafter (Fig. 17.2b). One major radiometabolite of ^{11}C-PBB3 appeared very quickly in the plasma and slowly decreased thereafter (Fig 17.2b). Both plasma parent and metabolite TACs in ADs and HCs were very similar (Fig. 17.2b)

Graphical plots (Eq. 17.4) with a combined $C_a^P(t) + C_a^M(t)$ plasma input became linear beyond t* = 11 min when both α and β could be considered constant. BP^*_{ND} estimations were very stable for all regions. On the other hand, the 2T kinetic analysis to estimate BP_{ND} was unstable in some regions with a large parameter estimation variability in the rest of the regions. The 2TC BP_{ND} values were numerically quite different from the corresponding BP^*_{ND} values with a very poor correlation between the two-tissue ratio minus 1 estimations ($BP_{ND} = 1.06 \pm 0.66$ vs. $BP^*_{ND} = 0.36 \pm 0.07$ with $r^2 = 0.04$ in the high binding region, for example.

The reference tissue model $MRTM_O$ robustly estimated BP^*_{ND} for the ROI data and enabled stable voxel-wise parametric imaging of BP^*_{ND}. The BP^*_{ND} estimated by the ROI-based $MRTM_O$ analysis closely matched the corresponding BP^*_{ND}

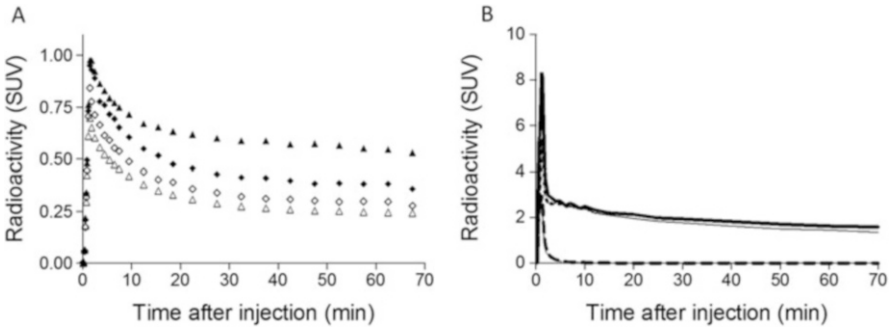

Fig. 17.2 Time activity curves (TACs) in the brain (**a**) and arterial plasma (**b**) after the injection of ^{11}C-PBB3 in AD patients and healthy controls (HCs). (**a**) TACs are shown for the high tau binding (▲) cerebral cortical region and cerebellar cortex (◆) in ADs, and the cerebral cortical region (△) and the cerebellar cortex (◇) in HCs. (B) Plasma TACs are shown for the total radioactivity (thick (ADs) and thin (HCs) solid lines), metabolite (thick (ADs) and thin (HCs) dotted lines), and parent (thick (ADs) and thin (HCs) dashed lines). Data represent mean of all 7 ADs or 7 HCs

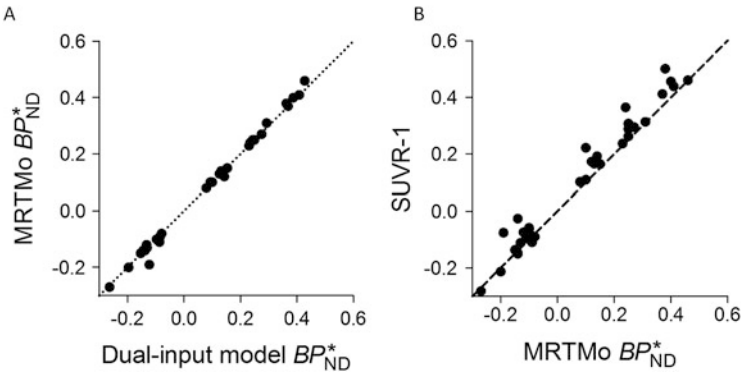

Fig. 17.3 (**a**) Correlation of ROI BP^*_{ND} estimated by dual-input graphical model and reference tissue model $MRTM_O$. (**b**) Correlation of ROI BP^*_{ND} estimated by $MRTM_O$ and SUVR minus 1 (50 min–70 min)

estimated by the dual-input graphical analysis with a perfect correlation between the two ($r^2 = 1.00$) (Fig. 17.3a). On the other hand, SUVR minus 1 values (calculated from the averaged 50 min to 70 min data) overestimated $MRTM_O$ BP^*_{ND} values by up to 38%. However, there was an excellent correlation between the two ($r^2 = 0.97$) (Fig. 17.3b). Both the $MRTM_O$ BP^*_{ND} parametric images and SUVR minus 1 images showed a clear delineation of tau pathology in the cerebral cortices including the hippocampal formation in AD (Fig. 17.4a, c) compared with HC (Fig. 17.4b, d).

17.4 Discussion

In the present article, we have shown that the reference tissue model-based binding potential (BP_{ND}) that reflects the target binding site density (B_{avail}) is theoretically equivalent to the tissue ratio minus 1 at equilibrium, whereas closely related SUVR minus 1 is the tissue ratio minus 1 at a fixed time point after the bolus radioligand administration. We have shown that the tissue ratio minus 1 at equilibrium (BP^*_{ND}) also reflects B_{avail} even in the situation where the radiometabolite enters the brain. The definition of binding potential, BP_{ND}, therefore can be extended to this situation (expressed as BP^*_{ND} here). The validity of the reference tissue model BP^*_{ND} and SUVR, both of which do not require arterial plasma data, can be evaluated by the dual-input $\left(C_a^P(t) + C_a^M(t)\right)$ model but not by the conventional single input ($C_a^P(t)$) model because the tissue ratio minus 1 at equilibrium includes the radiometabolite contribution to the tissue activity, which is not accounted for by the parent-only model. Of note is that the reference tissue BP^*_{ND} or SUVR estimation

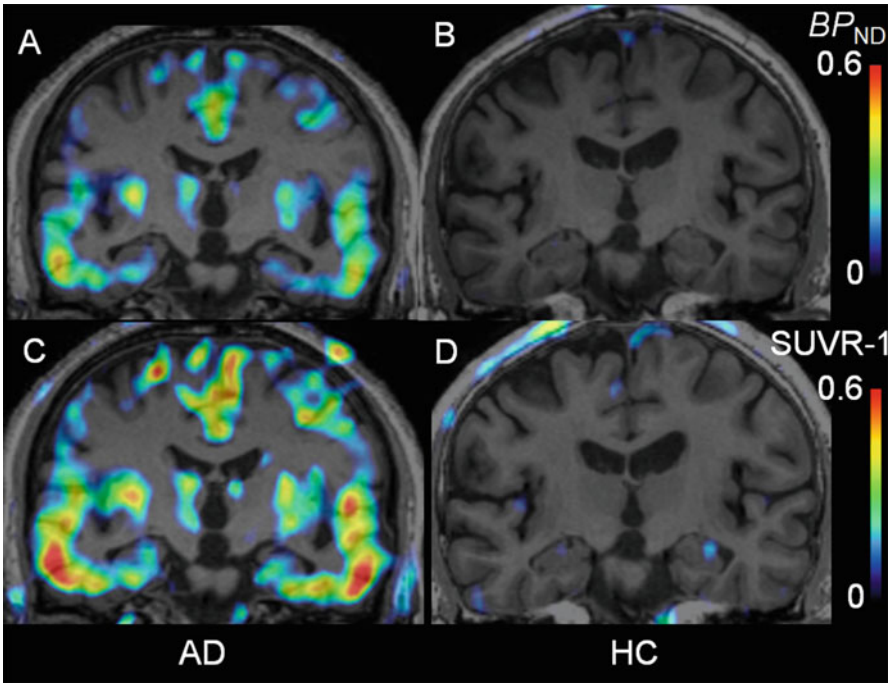

Fig. 17.4 Coronal parametric images of AD and HC. The $MRTM_O$ BP^*_{ND} images in ADs (**a**) and HCs (**b**). SUVR-1 images (50 min–70 min) in ADs (**c**) and HCs (**d**)

does not require any assumption of metabolite, because the estimation is performed without blood data.

Although we assumed here that the radiometabolite does not bind to the target site, it can be shown that BP_{ND} is also directly proportional to B_{avail} when the metabolite binds specifically (17.2). BP^*_{ND} has additional term, δV^M_{ND}, in the denominator (Eq. 17.2), which may increase the intersubject variability of BP^*_{ND} compared with BP_{ND}. In our ^{11}C-PBB3 analyses, there was no difference in the mean $\left(V^P_{ND} + \delta V^M_{ND}\right)$ values between ADs and HCs [2].

SUVR minus 1 at 50 min–70 min overestimated BP^*_{ND}. However, there was an excellent correlation between the two. SUVR is potentially affected by blood flow and systemic radioligand clearance, while BP^*_{ND} is independent of these factors because BP^*_{ND} represents the tissue ratio minus 1 at equilibrium. Therefore, a larger variability of cerebral blood flow in AD patents than in normal elderly subjects may result in a larger intersubject SUVR variability compared with BP^*_{ND}, although a longer dynamic imaging needed for BP^*_{ND} estimation might be less well tolerated for elderly patients than a shorter static imaging for SUVR measurements. The advantage of the reference tissue model-based estimation of the tissue ratio over the SUVR measurement has recently been shown for a long-term longitudinal Aβ PET imaging study [12].

17.5 Conclusions

The reference tissue-based binding potential (BP_{ND}) that reflects the target binding site density (B_{avail}) is equivalent to the tissue ratio minus 1 at equilibrium. The tissue ratio minus 1 at equilibrium (BP^*_{ND}) also reflects B_{avail} even in the situation where the radiometabolite enters the brain. The validity of the reference tissue model BP^*_{ND} and SUVR can be evaluated by the dual-input model not by the conventional single input model because the tissue ratio minus 1 at equilibrium includes the radiometabolite contribution to the tissue activity, which is not accounted for by the parent-only model.

References

1. Maruyama M, Shimada H, Suhara T, et al. Imaging of tau pathology in a tauopathy mouse model and in Alzheimer's patients compared to normal controls. Neuron. 2013;79:1094–108.
2. Kimura Y, Ichise M, Ito H, et al. PET quantification of tau pathology in human brain with ^{11}C-PBB3. J Nucl Med. 2015;56:1359–65.
3. Ichise M, Fujita M, Seibyl JP, et al. Graphical analysis and simplified quantification of striatal and extrastriatal dopamine D2 receptor binding with [^{123}I]epidepride SPECT. J Nucl Med. 1999;40:1902–12.
4. Ichise M. Neuroreceptor imaging and kinetic modeling. In: Van Heertum RL, Tikofsky R, Ichise M, editors. Cerebral SPECT and PET imaging. 4th ed. Philadelphia: Lippincott Wiliams and Wilkinson; 2009. p. 40–53. chapter 4.
5. Innis RB, Cunningham VJ, Delforge J, et al. Consensus nomenclature for in vivo imaging of reversibly binding radioligands. J Cerebr Blood F Met. 2007;27:1533–9.
6. Michaelis L, Menten ML. Die Kinetik der Invertinwirkung. Biochem Z. 1913;49:1333.
7. Braak H, Braak E. Neuropathological staging of Alzheimer-related changes. Acta Neuropathol. 1991;82:239–59.
8. Hashimoto H, Kawamura K, Igarashi N, et al. Radiosynthesis, photoisomerization, biodistribution, and metabolite analysis of ^{11}C-PBB3 as a clinically useful PET probe for imaging of tau pathology. J Nucl Med. 2014;55:1532–8.
9. Shimada H, Higuchi M, Shinotoh H, et al. In vivo visualization of tau pathology in Alzheimer's disease patients by [11C]PBB3-PET. Alzheimer's Dement. 2013;9:P845. Abstract.
10. Ichise M, Ballinger JR, Golan H, et al. Noninvasive quantification of dopamine D2 receptors in humans with iodine-123-IBF SPECT. J Nucl Med. 1996;37:513–20.
11. Herrmann M, Golombowski S, Kräuchi K, et al. ELISA-quantitation of phosphorylated tau protein in the Alzheimer's disease brain. Eur Neurol. 1999;42:205–10.
12. van Berckel BNM, Ossenkoppele R, Tolboom N, et al. Longitudinal amyloid imaging using ^{11}C-PiB: methodologic considerations. J Nucl Med. 2013;54:1570–6.

Chapter 18
Hypoxia Imaging with ^{18}F-FMISO PET for Brain Tumors

Kenji Hirata, Kentaro Kobayashi, and Nagara Tamaki

Abstract Tumor hypoxia is an important object for imaging because hypoxia is associated with tumor aggressiveness and resistance to radiation therapy. Here, ^{18}F-fluoromisonidazole (FMISO) has been used for many years as the most commonly employed hypoxia imaging tracer. Unlike F-18 fluorodeoxyglucose (FDG), FMISO does not accumulate in normal brain tissue making it able to provide images of hypoxic brain tumors with high contrast. Clinical evidence has suggested that FMISO PET can predict patient prognosis and treatment response. Among gliomas of various grades (WHO 2007), it has been known that grade IV glioblastoma resides under severe hypoxia and is a cause of development of necrosis in the tumor. For this study we tested whether FMISO can distinguish the oxygen condition of glioblastomas and lower-grade gliomas. Twenty-three glioma patients underwent FMISO PET for the study. All the glioblastoma patients ($N = 14$) showed high FMISO uptakes in the tumor, whereas none of the other patients (i.e., gliomas of grade III or lower, $N = 9$) did, demonstrated by both qualitative and quantitative assessments. The data suggest that FMISO PET may be a useful tool to distinguish glioblastomas from lower-grade gliomas. Our results, however, were slightly different from previous investigations reporting that some lower-grade gliomas (e.g., grade III) showed positive FMISO uptake. Many of these acquired the FMISO PET images 2 h after the FMISO injection, while for the study here we waited 4 h to be able to collect hypoxia-specific signals rather than perfusion signals as FMISO clearance from plasma is slow due to its lipophilic nature. No optimum uptake time for FMISO has been established, and we directly compared the 2-h vs. the 4-h images with the same patients ($N = 17$). At 2 h, the gray matter had significantly higher standardized uptake value (SUV) than the white matter, possibly due to different degrees of perfusion but not due to hypoxia. At 4 h, there were no differences between gray and white matter without any significant increase in the noise level measured by the coefficient of variation between the 2-h and the 4-h images. At 2 h, 6/8 (75 %) of glioblastoma patients

K. Hirata (✉) • K. Kobayashi
Department of Nuclear Medicine, Hokkaido University, Sapporo, Japan
e-mail: khirata@med.hokudai.ac.jp

N. Tamaki
Department of Nuclear Medicine, Graduate School of Medicine, Hokkaido University, Sapporo, Japan

Y. Kuge et al. (eds.), *Perspectives on Nuclear Medicine for Molecular Diagnosis and Integrated Therapy*, DOI 10.1007/978-4-431-55894-1_18

showed higher uptakes in the tumor than in the surrounding brain tissue, whereas at 4 h this was the case for 8/8 (100 %). In addition, at 2 h, 3/4 (75 %) of patients with lower-grade gliomas showed moderate uptakes, while at 4 h none did (0/4 or 0 %). These data indicate that 4-h images are better than 2-h images for the purpose of glioma grading. In conclusion, we evaluated the diagnostic performance of FMISO PET for gliomas and suggest that FMISO PET may be able to assist in the diagnosis of glioblastomas when PET images are acquired at 4 h post injection.

Keywords Hypoxia • 18 F-Fluoromisonidazole • Glioma • Glioblastoma

18.1 Introduction

This review article summarizes our recent studies with ^{18}F-fluoromisonidazole (FMISO) positron emission tomography (PET) applied to brain tumors [1, 2]. A variety of tumors which can be divided into two categories develop in the brain: primary brain tumors that originate from the brain tissue and metastatic brain tumors that originate from malignant tumors in other organs. Gliomas account for 60 % of primary brain tumors. Gliomas comprise a range of tumors, from benign to malignant, that are derived from glial cells such as astrocytes, oligodendrocytes, and ependymal cells. Among gliomas, the glioblastoma is the most aggressive astrocytic tumor. Glioblastomas are categorized as grade IV in the WHO classification [3]. The standard treatment for glioblastomas is surgery followed by radiotherapy and chemotherapy [4]. With state-of-the-art multidisciplinary therapy, the 1-year survival rate of glioblastoma patients is reported to be 56 %, which is significantly poorer than with grade III (78 %) or less malignant gliomas [5]. A pathological diagnosis of surgical specimens by biopsy or resection is necessary to establish the diagnosis for glioblastomas [6], but brain surgery involving eloquent regions can exacerbate the prognosis by causing neurological morbidity and should be avoided if possible [7]. Patients with impaired performance status or elderly patients especially would benefit from nonsurgical methods of establishing the diagnosis, substituting surgical tissue sampling.

The basic in vivo imaging modality for brain tumors is magnetic resonance (MR) imaging. Intratumoral characteristics and tumor expansion states are shown accurately with MR imaging. The use of PET with ^{18}F-fluorodeoxyglucose (FDG) is a well-established method for many different types of tumors in the body, including lung cancer, head and neck cancers, and others. FDG PET also plays important roles in the diagnosis of glioblastomas. The diagnosis of a glioblastoma is generally suggested if there is a ringlike enhancement by gadolinium on MR images or an intense uptake of FDG [6, 8–15]. However, there are cases of false-negative MRI findings as some glioblastoma lack the ringlike enhancement [6]. In discriminating glioblastoma from grade III tumors, FDG PET is also not always adequate as a large number of patients of grade III gliomas show high FDG uptakes [13, 14]. This makes a biopsy necessary in many cases, and a noninvasive in vivo imaging tool would be of benefit to omit invasive biopsy procedures in clinical settings [11].

The WHO 2007 criteria determine the glioma grade based on microscopic characteristics present in the malignancy. Grade II tumors show cell atypia and grade III tumors tissue anaplasia and cell mitosis in addition to cell atypia. Grade IV glioblastomas have pathological features that are not found in grade III or lower-grade gliomas, particularly microvascular proliferation and necrosis [3]. Basically, necrosis is considered to be closely related to hypoxia as low oxygen concentrations do not allow the energy metabolism to proceed as in unaffected tissue. In fact, glioblastomas are known to be in a state of severe hypoxia possibly due to vascular abnormalities and high oxygen demand, whereas the hypoxia of grade III or lower-grade gliomas is less severe [16–19]. We hypothesized that imaging the hypoxia of glioblastomas could be useful to distinguish glioblastomas from lower-grade gliomas.

Measuring hypoxia in living tissue uses needle electrodes; however, this technique presents significant shortcomings. First, it is invasive to insert a needle into deep layers of tissue in humans. Second, it requires considerable skill and the reproducibility is not high. Third, needles may alter the tissue structure and so influence the local oxygen partial pressure, and for these reasons needle electrodes are not used in clinical practice. An alternative is presented by ^{18}F-fluoromisonidazole (FMISO) PET which is a widely used method for in vivo hypoxia imaging [20–23]. Valk et al. first introduced the use of FMISO for glioma imaging in 1992 [24], and the usefulness of FMISO for glioma imaging has been extensively investigated [25–32]. The FMISO is also known to accumulate in severe hypoxic structures but not in mildly hypoxic structures, suggesting that FMISO would be able to discriminate severe from mild hypoxia. This made us hypothesize that much FMISO may accumulate in glioblastomas and only little in lower-grade gliomas. If such a difference could be substantiated, hypoxia imaging using FMISO would provide an avenue to discriminate glioblastomas from lower-grade gliomas. The first paper of our project was to test the hypothesis [1]. We evaluated the diagnostic usefulness of FMISO PET in terms of glioma grading in comparison with diagnosis with FDG PET in patients suspected of having glioblastomas on MR images.

With FMISO there is a trade-off problem regarding uptake time (the interval between the FMISO injection and the PET emission scanning). A longer uptake time is theoretically desirable to image hypoxia with good lesion-to-background signal ratios, but the longer time leads to lower signal-to-noise ratios due to radiological decay of the F-18. Early reports by Grunbaum et al. [33] and Thorwarth et al. [34] addressing this issue suggested a 4-h acquisition as suitable. Despite this, most research adopted 2-h protocols [24, 25, 27–32], possibly because a shorter protocol would be more generally acceptable in clinical settings. Based on this, the second part of our project was to directly compare 2-h and 4-h images from the same patients [2].

18.2 Materials and Methods

The first of the studies reported here was conducted for the purpose of testing the ability to discriminate between glioblastomas and lower-grade gliomas with FMISO PET. Twenty-seven patients with possible high-grade gliomas were considered for the study [1]. The patients included showed cerebral parenchymal tumors surrounded by edematous tissue on MR images but no known malignancy in other organs. We excluded patients where previous tumorectomy, chemotherapy, or radiotherapy for lesions had been performed. The only exception was a patient with a recurrent tumor 6 years after tumorectomy combined with chemoradiotherapy for a low-grade glioma. Among the 27 patients, two were excluded because they had contraindications of surgical operations. The remaining 25 patients underwent either a tumoral resection ($n = 16$) or biopsy ($n = 9$) at most 2 weeks after the PET scanning. The surgical specimen was investigated by two experienced neuropathologists to determine the pathological diagnosis based on the 2007 WHO classification. Among the 25 patients, two were diagnosed as having metastatic adenocarcinoma and multiple sclerosis, respectively, and these two patients were excluded from the analysis. Finally 23 patients (M/F = 10:13, age 57 ± 15 years old) all with the pathological diagnosis of gliomas were included in the study.

With these 23 patients, we acquired FMISO and FDG PET images following the same protocol for all the patients. The interval between FMISO and FDG was at most 1 week. The FMISO synthesis protocol was previously described in detail elsewhere [35, 36]. On the day of FMISO, the patient was not asked to fast before the PET, and 400 MBq of FMISO was intravenously injected. Then, 4 h later, the emission scanning was initiated to acquire static PET images of the entire brain. FDG PET was performed on another day; here the dosage of FDG was also 400 MBq. The uptake time for FDG was 1 h, and the scanning range for the FDG PET was the same for the FMISO PET with a high-resolution PET scanner (ECAT HR+ scanner; Asahi-Siemens Medical Technologies Ltd., Tokyo, Japan) operated in a three-dimensional mode for 22 patients. For one patient the FMISO images were acquired using an integrated PET-CT scanner (Biograph 64 PET-CT scanner; Asahi-Siemens Medical Technologies Ltd., Tokyo, Japan). The duration of the emission scanning using the ECAT HR+ scanner was 10 min. The duration of the transmission scanning using the ECAT HR+ scanner with a ^{68}Ge/^{68}Ga retractable line source was 3 min. This acquisition protocol was the same for both FDG and FMISO. With the Biograph 64 PET-CT scanner, the duration of the emission scanning was also 10 min. The transmission scanning was performed using an X-ray CT, and the attenuation correction used the CT images. The attenuation-corrected radioactivity images from both scanners were reconstructed using a filtered back projection with a 4 mm full width at half maximum Hann filter.

For our second study, to compare the 2-h vs. 4-h images of FMISO PET, we investigated 17 different patients with brain tumors (M/F = 7:10, age 62 ± 14 years old, range 33–85 years old). The study populations for first and second studies were

different, and none of the patients included in the first study were included in the second study. The PET images for each patient in the second study were acquired twice, 2 and 4 h following the injection. The injected dosage of FMISO was 399 ± 25 MBq. The first scanning took place 115.9 ± 14.6 min after the injection and the second 227.4 ± 15.1 min after injection. The scanner was a Gemini GXL 16 PET-CT (Philips). The duration of the emission scanning was 20 min. Transmission scanning was performed using the X-ray CT which was used for attenuation correction. Attenuation-corrected radioactivity images were reconstructed using ordered subset expectation maximization.

For the first study, the images were analyzed both qualitatively and quantitatively. An experienced nuclear physician who was blinded from the pathological diagnosis visually evaluated all the images in the qualitative assessment for the first study. In the qualitative assessment of the FMISO PET images, the FMISO uptake was visually categorized into three groups. Where the highest uptake in the tumor was weaker than that in the surrounding brain tissue, the patient was considered as showing *low FMISO uptake*. Where the highest uptake in the tumor was equal to that in the surrounding brain tissue, the patient was considered as showing *intermediate FMISO uptake*. Where the highest uptake in the tumor was stronger than that in the surrounding brain tissue, the patient was considered as showing *high FMISO uptake*. This grouping rule was however not efficient as no patients were assigned to show *low FMISO uptake*. As a result the *low FMISO uptake* and the *intermediate FMISO uptake* patients were combined in one group of *FMISO-negative* patients. The remaining patients, those assigned to the *high FMISO uptake* group, were designated as *FMISO-positive* patients. This binary division was presented in a previous paper [27]. Similarly, in the qualitative assessment of the FDG PET images, we evaluated the FDG accumulation in the tumor using the grouping detailed elsewhere [14]. First, the FDG uptake was visually categorized into three groups: low, intermediate, and high. Where the highest uptake in the tumor was weaker than or equal to that in the contralateral white matter, the patient was considered as showing *low FDG uptake*. Where the highest uptake in the tumor was stronger than that in the contralateral white matter but weaker than that in the contralateral gray matter, the patient was considered as showing *intermediate FDG uptake*. Where the highest uptake in the tumor was equal to or stronger than that in the contralateral gray matter, the patient was considered as showing *high FDG uptake*. Like the FMISO categorization, the *low FDG uptake* and *intermediate FDG uptake* patients were combined and termed *FDG-negative* patients, and those of *high FDG uptake* were termed FDG-positive patients.

For the second study, the grouping of the FMISO uptake in the tumor was performed slightly differently, here it was visually assessed. The degree of uptake was assigned as either high, medium, or low. Low uptake here means the uptake compared to the surrounding brain tissue.

Such qualitative assessments may be subjective and a quantitative assessment was also made. For the first study, the PET images were coregistered with individual MR images (FLAIR) using a mutual information technique implemented in the NEUROSTAT software package [37, 38]. Then, polygonal regions of interest

(ROI) were manually drawn to enclose the entire tumor on every slice that also included peritumoral edematous regions. The single voxel having the highest radioactivity concentration in the tumor was determined in the PET images using in-house software. The highest radioactivity concentration was used to calculate a maximum standardized uptake value (SUV_{max}). A SUV_{peak} value has recently come into use to overcome the shortcomings of SUV_{max}. However, the concept of SUV_{peak} is not unique as different researchers use different definitions. Here, we use the term SUV_{10mm} to explicitly show the meaning: a 10-mm-diameter circular ROI with the center at the maximum voxel was created. The averaged value for the circular ROI was assigned as SUV_{10mm}, and the SUV was calculated as (tissue radioactivity [Bq/ml])*(body weight [g])/(injected radioactivity [Bq]). Next, further ROIs were created on the following reference regions: the cerebellar cortex, the contralateral frontoparietal cortex on the level of the centrum semiovale, and the contralateral frontoparietal white matter on the level of the centrum semiovale. The lesion-to-cerebellum ratio of the FMISO was determined as the ratio of the SUV_{10mm} to the cerebellar averaged SUV. The lesion-to-gray matter and lesion-to-white matter ratios of the FDG were the ratios of SUV_{10mm} to gray matter and white matter SUV, respectively [13]. The ROI placement process was performed by an experienced nuclear physician, and where the tumor occupied bilateral lobes, the hemisphere with the larger part of the tumor was considered as the tumor side. We further measured the hypoxic tissue volume showing significant FMISO uptake in the tumor with the cerebellum used as the reference tissue for this purpose. The voxels having higher SUV than 1.3 times that of the cerebellar SUV were extracted in the tumoral polygonal ROI described above. No threshold for FMISO uptake volumes has been established, and the 1.3 value was empirically adopted from image segmentation in ^{11}C-methionine brain PET [31, 39, 40]. The FMISO uptake volumes were expressed as a percentage of the extracted voxels in the whole tumoral ROI.

For the second study, the 2-h and 4-h images were coregistered to CT. To obtain reference values from normal tissue, circular 10-mm-diameter ROIs were defined on gray matter, white matter, and the cerebellar cortex. The SUV_{mean}, standard deviation (SD), and coefficient of variation (CV) were measured within these ROIs. To express tumor uptake values, the SUV_{max} and lesion-to-cerebellum ratios were calculated in the same way as in the first study.

In the following, all parametric data are expressed as means $\pm$ SD. The patients with grade III or with less malignant gliomas were grouped together as non-glioblastoma patients to simplify the analysis. The relationship between the histopathological diagnosis and the visual assessment results was examined using Fisher's exact test. The differences in age, tumor size, SUVs, lesion-to-normal tissue ratios, and uptake volume for glioblastoma vs. non-glioblastoma patients were examined using the Mann-Whitney *U*-test. The 2-h vs. 4-h values were compared using paired t-tests; *P*-values smaller than 0.05 were considered statistically significant. The statistical analysis and figure drawing used R 2.14.0 and R 3.1.3 for Windows.

18.3 Results

In the first study, 14 patients were diagnosed with glioblastomas and categorized as grade IV in the WHO classification. Among the remaining nine patients, one had anaplastic astrocytoma (grade III), one had anaplastic oligodendroglioma (grade III), three had anaplastic oligoastrocytomas (grade III), one had diffuse astrocytoma (grade II), one had oligodendroglioma (grade II), and two had oligoastrocytomas (grade II). Necrosis was identified in all the glioblastoma patients, while none of the non-glioblastoma patients showed necrosis within the tumor. The age of the glioblastoma patients was 65.5 ± 9.9 years, and the age of non-glioblastoma patients was 43.7 ± 12.2 years; the age difference was statistically significant ($p < 0.01$). The tumor sizes were measured on FLAIR MR images and were not significantly different for glioblastomas vs. non-glioblastomas (64.4 ± 17.5 mm vs. 77.6 ± 22.5 mm in diameter) ($p =$ NS). Gadolinium enhancement was observed in 3/9 non-glioblastoma patients and in14/14 glioblastoma patients. By visual assessment, all of the glioblastoma patients (14/14) were classified as FMISO positive and all of the non-glioblastoma patients as FMISO negative. There was a significant association by Fisher's exact test between the histology (glioblastoma or non-glioblastoma) and FMISO uptake (FMISO positive or FMISO negative) ($p < 0.001$). This visual assessment of the FMISO PET images correctly discriminated glioblastoma patients from non-glioblastoma patients with sensitivity, specificity, and accuracy of 100 %, 100 %, and 100 %, respectively. For the FDG PET results, after excluding a diabetic patient with hyperglycemia at the time of the FDG PET, all glioblastoma patients (13/13) were FDG positive and 3/9 non-glioblastoma patients were FDG positive. This relationship reached statistical difference ($p < 0.01$), but the diagnostic performance of the FDG PET was poorer than the FMISO PET, with sensitivity, specificity, and accuracy being 100 %, 66 %, and 86 %, respectively. Figures 18.1, 18.2, 18.3, 18.4, and 18.5 show representative cases.

In the quantitative assessment of the first study, the SUV_{max} of the FMISO was 3.09 ± 0.62 (range, 2.22–4.31) in glioblastoma patients, significantly higher than in non-glioblastoma patients (1.73 ± 0.36; range, 1.36–2.39) ($p < 0.001$). As detailed above, we introduced the SUV_{10mm} term to be able to minimize noise effects. The SUV_{10mm} of FMISO was similar to the SUV_{max} of FMISO, with the values being 3.00 ± 0.61 (range, 2.15–4.18), significantly higher than in non-glioblastoma patients (1.64 ± 0.38; range, 1.29–2.35) ($p < 0.001$). The lesion-to-cerebellum ratio of the FMISO (the SUV_{10mm}/cerebellar SUV) was higher in the glioblastoma patients (2.74 ± 0.60; range, 1.71–3.81) than in the non-glioblastoma patients (1.22 ± 0.06; range, 1.09–1.29) ($p < 0.001$). The quantitative results of the FDG PET were slightly different from those of the FMISO PET. Here the diabetic patient was also excluded from the analyses of SUV and the lesion-to-normal tissue ratio of the FDG PET. The SUV_{max} of the FDG was not significantly different for the glioblastoma and non-glioblastoma patients (7.55 ± 3.72; range, 4.34–16.38, vs. 8.21 ± 6.04; range, 4.75–23.49) ($p = 0.95$). Similarly, the SUV_{10mm} of the

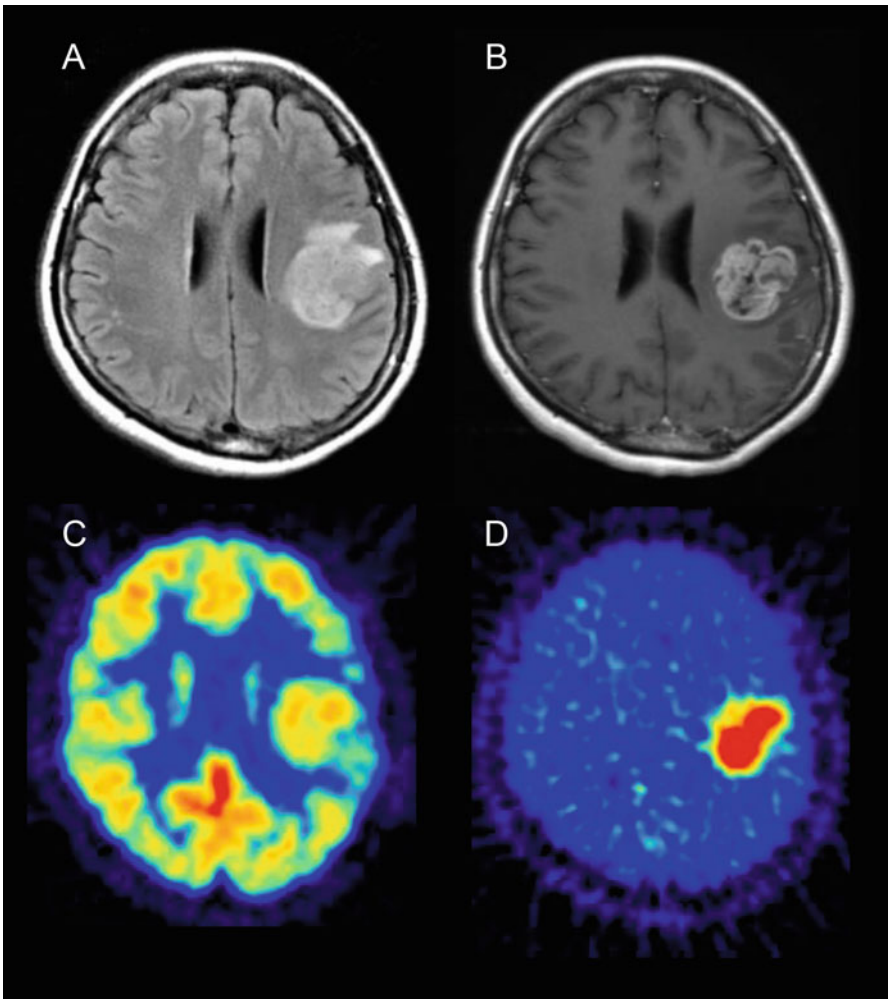

Fig. 18.1 A glioblastoma case. (**a**) The FLAIR image showed a high-signal tumor in the left hemisphere. (**b**) The tumor was enhanced by gadolinium contrast material. (**c**) The FDG uptake in the tumor was comparable to that of contralateral cerebral cortex. (**d**) The FMISO uptake was higher in the tumor than in the surrounding brain tissue

FDG was not significantly different for the glioblastoma and non-glioblastoma patients (7.41 ± 3.63; range, 4.26–15.90, vs. 8.03 ± 5.96; range, 4.64–23.12) ($p = 0.95$). The lesion-to-gray matter ratio of the FDG (the SUV_{10mm}/SUV in the contralateral gray matter) was higher in the glioblastoma patients (1.46 ± 0.75; range, 0.91–3.79) than in the non-glioblastoma patients (1.07 ± 0.62; range, 0.66–2.95, $p < 0.05$). The lesion-to-white matter ratio of the FDG (the SUV_{10mm}/SUV in the contralateral white matter) was not significantly different for the glioblastoma (2.81 ± 1.23; range, 1.87–6.44) and non-glioblastoma (2.66 ± 1.60;

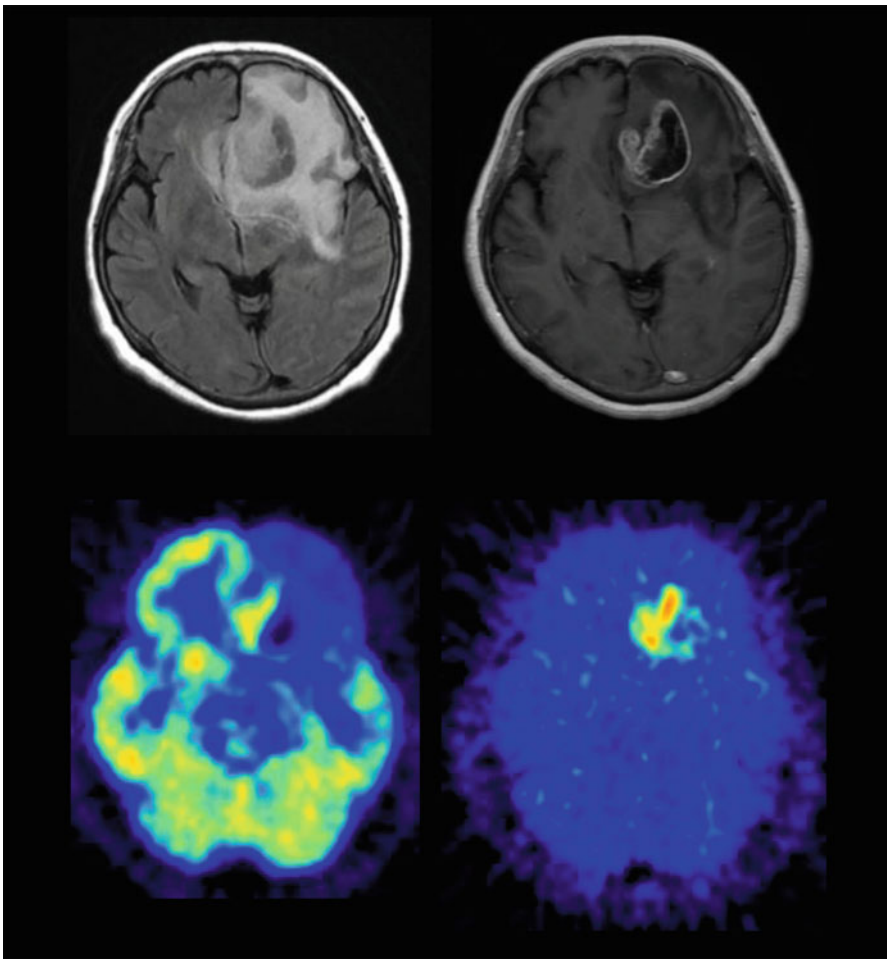

Fig. 18.2 A glioblastoma case. (**a**) The FLAIR image showed a tumor in the left frontal lobe. (**b**) The tumor showed a ringlike enhancement by gadolinium contrast material. (**c**) The FDG uptake was observed in a part of the gadolinium-enhanced area. The FDG uptake was comparable to the right cerebral cortex. (**d**) The FMISO PET showed a similar distribution of FMISO as FDG but with stronger tumor-to-background contrast than FDG

range, 1.71–6.51) ($p = 0.16$) patients. Finally, the uptake volume of FMISO was larger in the glioblastoma than in non-glioblastoma patients (27.18 ± 10.46 %; range, 14.02–46.67 %, vs. 6.07 ± 2.50 %; range, 2.12–9.22 %), ($p < 0.001$).

In the second study, the 2-h images and the 4-h images of FMISO PET were directly compared for the same subjects. Figure 18.6 shows representative images that do not show tumors. Visually, the SUV in the brain was higher at 2 h than at 4 h. More specifically, the gray matter SUV was higher at 2 h than at 4 h, whereas the white matter SUV was comparable in the images at 2 h and 4 h. Profile curves

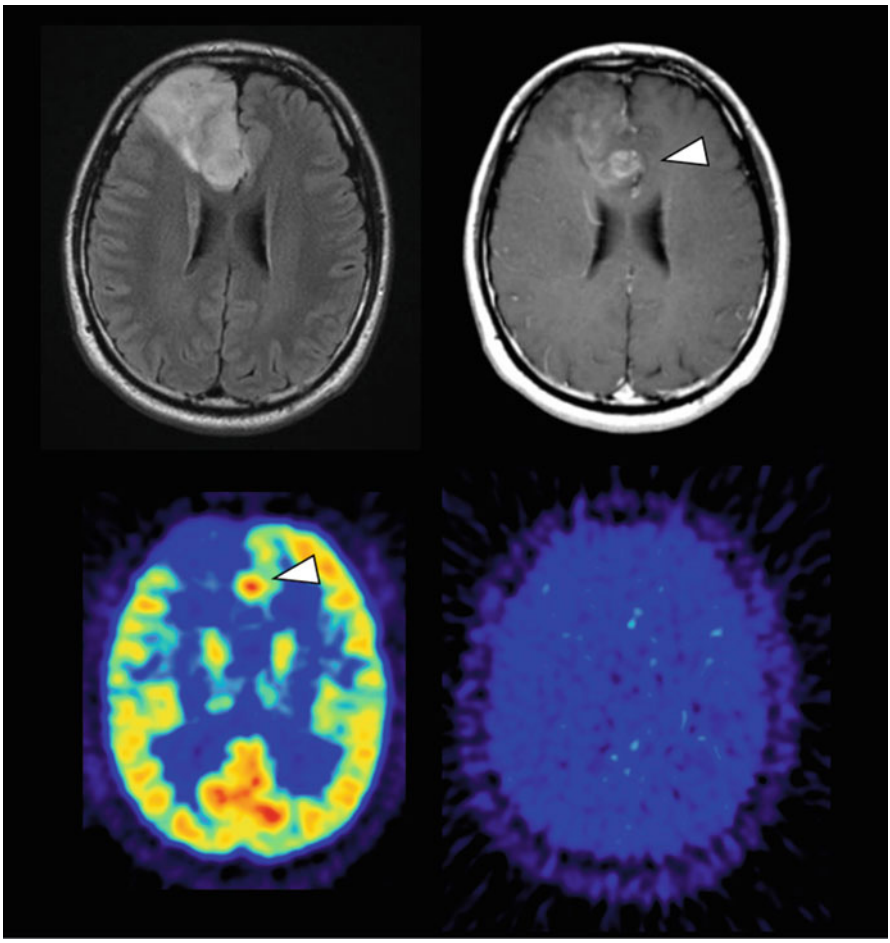

Fig. 18.3 An anaplastic oligoastrocytoma case (grade III). (**a**) The FLAIR image showed a tumor in the right frontal lobe. (**b**) A small part of the tumor is enhanced after treatment with gadolinium contrast material (arrowhead). (**c**) The FDG uptake was observed in the enhanced part (arrowhead). The FDG uptake was higher than that in the left cerebral cortex. (**d**) No FMISO accumulated in the tumor

demonstrate these differences in Figure 18.6. At 2 h, the gray matter was distinguishable from the white matter, as the gray matter showed higher SUV than the white matter while at 4 h; the curve was almost flat. Figure 18.7 shows scatter plots of gray and white matter SUV at 2 h vs. 4 h. In all cases the gray matter SUV decreased with time and all the points plot under the line of identity. White matter SUV was not significantly different at 2 and 4 h. Figure 18.8 shows the CV of gray and white matter, compared at 2 h and 4 h. The gray matter CV increased slightly from 2 to 4 h ($P = 0.0008$), while the white matter CV was not significantly different at 2 and 4 h.

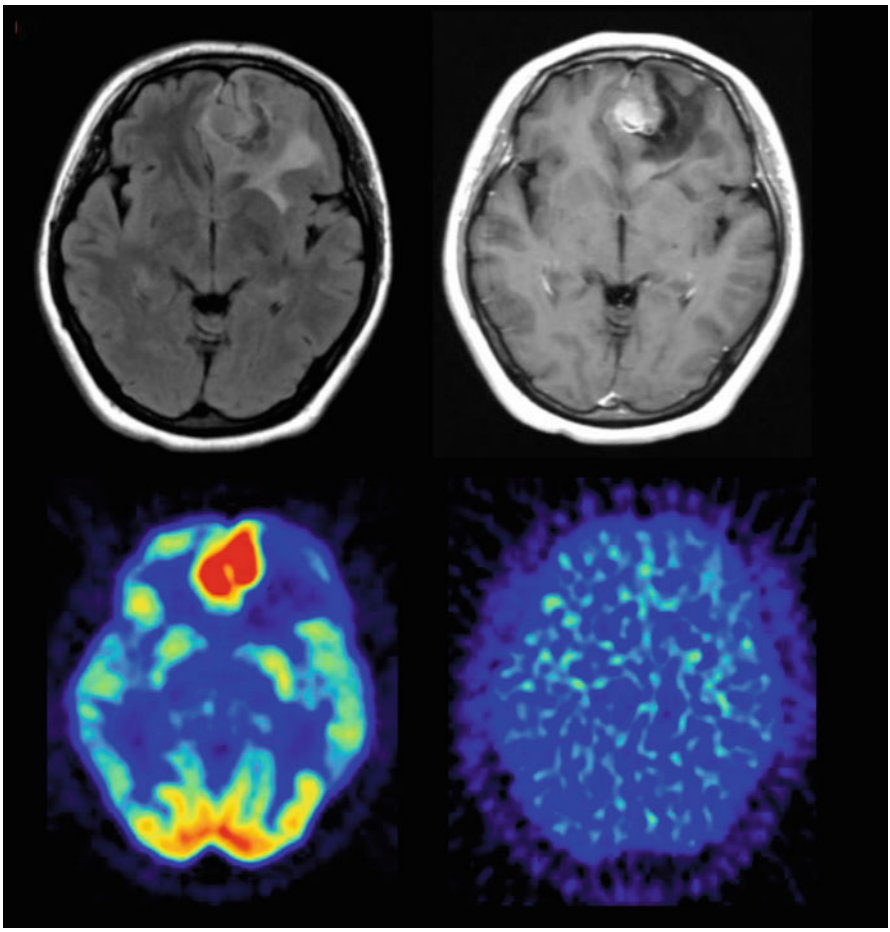

Fig. 18.4 An anaplastic oligodendroglioma case (grade III). (**a**) The FLAIR image showed a tumor in the left frontal lobe. (**b**) A part of the tumor enhanced by gadolinium contrast material. (**c**) The FDG uptake was observed even outside the enhancing area. The FDG uptake was much higher than that in the right cerebral cortex. (**d**) No FMISO uptake was observed in the tumor

In the visual assessment of the tumors, we first looked into grade IV tumors because based on the first study we believed that the grade IV tumors would have a hypoxic volume and thus should show FMISO uptake. At 2 h, six out of eight grade IV patients showed high FMISO uptakes, and the remaining two patients showed medium uptakes. At 4 h, however, eight out of eight (100 %) patients showed high FMISO uptakes. Then, we looked into grade II and III tumors that we thought would not have developed severe hypoxia and thus would not show FMISO uptake. At 2 h, three out of four patients showed medium uptakes and the fourth patient showed a low uptake. This was changed at 4 h where four out of four (100 %) patients showed low uptakes. The results of the visual assessment can be

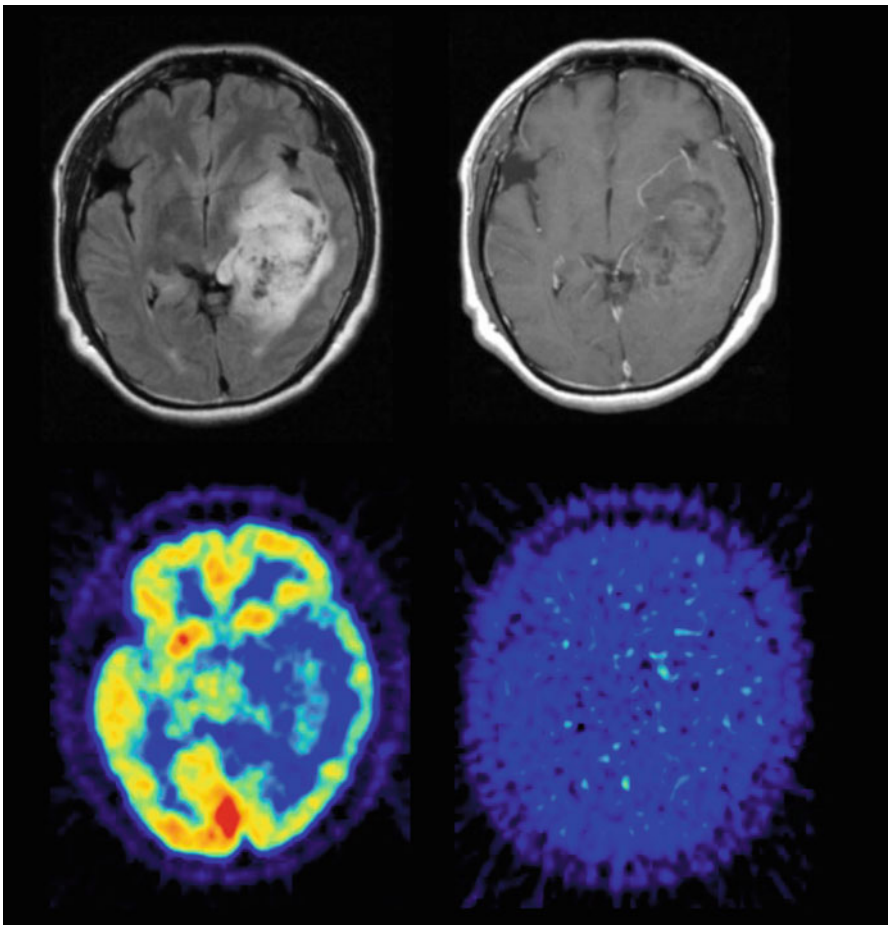

Fig. 18.5 An oligodendroglioma case (grade II). (**a**) The FLAIR image showed a tumor in the left temporal lobe. (**b**) The tumor slightly enhanced by gadolinium contrast material. (**c**) The FDG uptake was weaker than in the right cerebral cortex. (**d**) No FMISO uptake was observed in the tumor

summarized as those 4-h images provide more definitive information for discriminating grade IV tumors from lower-grade tumors. The quantitative analysis further supported this; in all the cases, the SUV_{max} and tumor-to-normal ratio increased from 2 h to 4 h (Fig. 18.9). Here, lower-grade gliomas (grades II and III) showed decreases in SUV_{max} and in the tumor-to-normal ratio from 2 h to 4 h (Fig. 18.10).

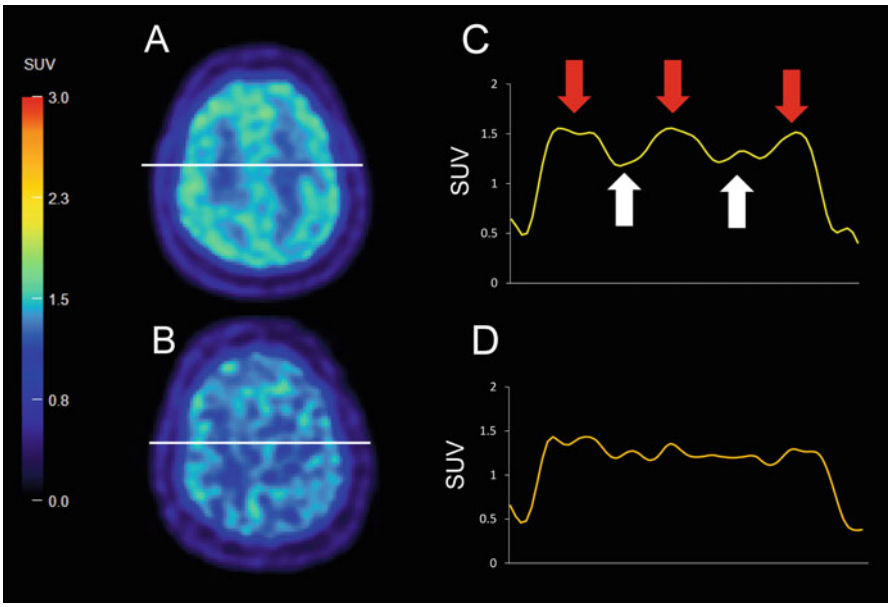

Fig. 18.6 A brain slice FMISO PET image (**a**) 2 h after administration of FMISO and (**b**) after 4 h. No tumor existed on these slices. (**c**) 2-h SUV profile corresponding to the horizontal line in (**a**). The red arrows indicate gray matter, and the white arrows indicate white matter. (**d**) 4-h profile corresponding to the horizontal line (**b**)

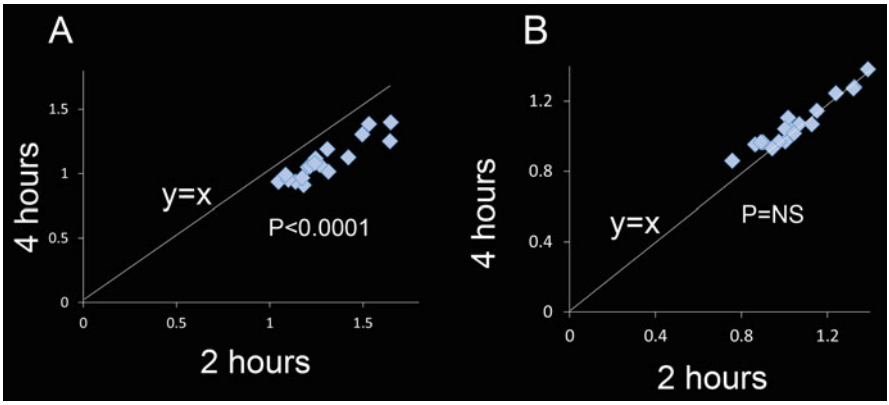

Fig. 18.7 SUV of (**a**) gray and (**b**) white matter at 2 h vs. 4 h

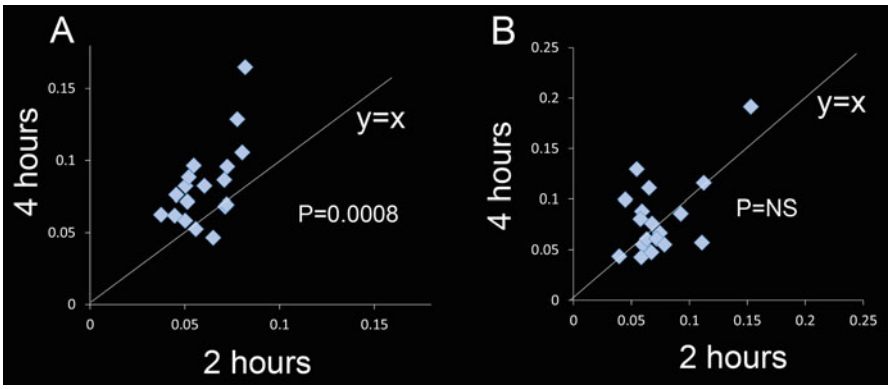

Fig. 18.8 Plot of variation (CV) of (**a**) gray and (**b**) white matter at 2 h vs. 4 h

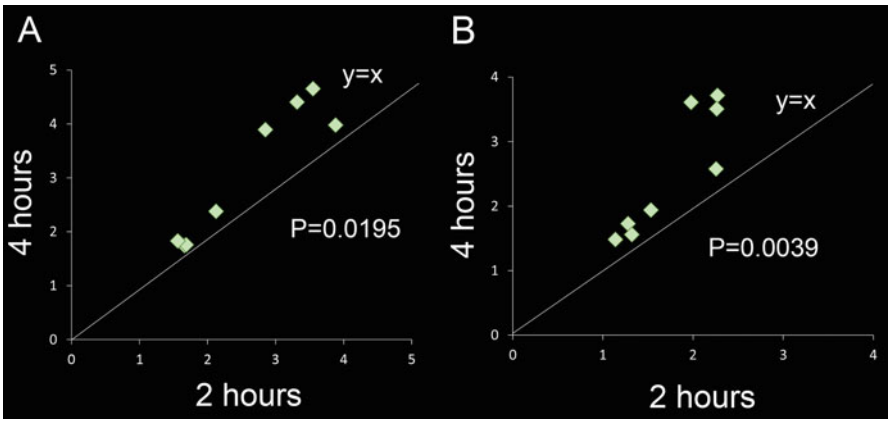

Fig. 18.9 All glioblastoma cases showed increases in both the (**a**) SUV_{max} and (**b**) tumor-to-normal ratio from 2 h to 4 h

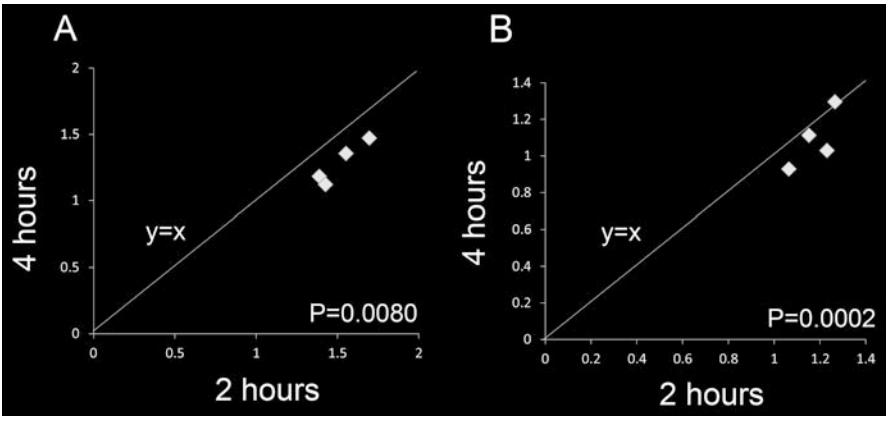

Fig. 18.10 All grade II to III cases showed decrease in (**a**) SUV_{max}, and 3/4 cases showed decrease in (**b**) tumor-to-normal ratio from 2 h to 4 h

18.4 Discussion

We have detailed two studies in this article. The results of the first indicated that much FMISO accumulated in all the glioblastomas here but not in the lower-grade gliomas. Different from this, FDG accumulated in both glioblastomas (100 %) and in some lower-grade gliomas (33 %). This suggests that FMISO PET is superior to FDG PET in a differential diagnosis. Visual analysis was confirmed by analyses of the SUV, lesion-to-normal tissue ratio, and FMISO uptake volume. The results of the second study indicated that FMISO PET 4 h after administration is superior to the images after 2 h in differentiating glioblastomas from non-glioblastomas.

In the 2007 WHO definition, grade IV gliomas show microvascular proliferation and necrosis as well as anaplasia and mitotic activity [3]; necrotic tissue is not observed in grade III or lower-grade gliomas. In brain tumor specimens, necrotic change is an important histopathological landmark that distinguishes glioblastomas from lower-grade gliomas. In previous reports, the necrosis in glioblastoma is considered to be associated with tissue hypoxia [16, 17]. The FMISO PET identification of hypoxia proceeds through several steps. Injected FMISO is first transported by the blood flow and taken up by viable cells. Then, FMISO is oxidized by intracellular oxygen if there is a sufficient amount of oxygen available in a cell, and the oxidized FMISO is excreted from the cell. The FMISO is not oxidized when there is insufficient oxygen available (hypoxic conditions) and the FMISO is here retained in the cell [41]. Considering these mechanisms, we may expect that FMISO accumulates in perinecrotic hypoxic tissue but not in the central necrotic region. We observed that only little FMISO accumulates in non-glioblastoma patients. Some studies used needle electrodes to measure oxygen partial pressures in human gliomas [18, 19, 42] and have suggested that both glioblastomas and grade II and III gliomas are present under hypoxic conditions. Lower-grade gliomas do not develop necrosis and may be expected to suffer from only a milder degree of hypoxia than that of glioblastomas [18, 19]. FMISO accumulation requires severe hypoxic conditions ($pO2 < 10$ mmHg) [43, 44], and the results here are consistent with this.

Cher et al. investigated FMISO uptake in various tumors and the correlation with histological findings [27]. They reported that all grade IV tumors showed high FMISO uptakes (they were FMISO positive as we define it here) and that all grade I and II tumors showed FMISO uptakes comparable to the surrounding tissue (they were FMISO negative as we define it). However, there was a slightly elevated FMISO uptake in one of three grade III patients and low uptakes in the remaining two grade III patients [27]. Our results in the first study are consistent with this previous data, except for the grade III patients, as all of our grade III gliomas were FMISO negative. Cher et al. used 2 h as the waiting time before conducting the FMISO PET scanning, while the study here used 4 h. Many FMISO PET protocols have used 2 h as the uptake time [24, 25, 27–32], while Thorwarth et al. questioned the adequacy of 2 h for imaging of FMISO [34]. There, the kinetic analysis of dynamic datasets of FMISO PET suggested that the hot spots at 2 h did not reflect

actual hypoxia but rather showed a high initial influx of the FMISO due to increased blood flow to the tumor. In our first study, no grade III patients showed high FMISO uptakes, and we speculated that this was possibly because the relatively long uptake time allowed the tracer to be excreted from the tissue without severe hypoxia. To further elucidate this, we conducted the second study, to directly compare images at 2 and 4 h after FMISO injection in the same patients. At 4 h, the background gray matter SUV was lower, and the presence of the tumor uptake was fully substantiated: all the glioblastomas were FMISO positive, and all the non-glioblastomas were FMISO negative. These results are consistent with the Thorwarth observations [34].

Recent advances in molecular targeting therapies and image guided therapies are remarkable, and it may be expected that in the near future the therapy of first choice for glioblastomas will be chemo- or radiotherapy rather than surgery. In such cases, new techniques like FMISO PET may help avoid a biopsy followed by a pathological investigation. Aged patients or patients with impaired performance status would particularly benefit from such techniques.

The FDG PET reflects the histological aggressiveness of gliomas, and glioblastomas commonly show the highest FDG uptake among gliomas [12–14]. In the first study here, a high FDG uptake was unexceptionally observed in glioblastoma patients. At the same time, however, three of nine non-glioblastoma patients also showed high FDG uptakes. These findings are consistent with the previous data [13, 14], and the results indicate that FDG PET is useful for histological grading but inconclusive when a differential diagnosis of glioblastomas from lower-grade gliomas is at issue. This leads us to suggest that FMISO PET may play a more important role when a tumor shows a high FDG uptake (equal to or greater than the uptake in the surrounding gray matter). Another important PET tracer for brain tumor imaging is ^{11}C-methionine (MET). For MET the uptake intensity corresponding to each tumor grade can be summarized as in Fig. 18.11. It is well

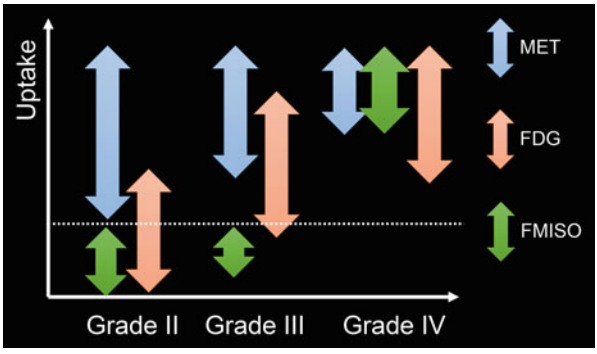

Fig. 18.11 A scheme of the suggested roles of ^{11}C-methionine (MET), ^{18}F-FDG, and ^{18}F-FMISO PET in differential diagnosis of gliomas

known that even grade II tumors may show high MET uptakes, especially in the case of tumors with oligodendroglial components [45, 46], and that MET is good at showing the tumor boundary. The FDG uptake increases with the tumor grade [47], and the results here suggest that FMISO uptake is absent in grades II and III, but strong in grade IV. Altogether these tracers will provide significant information to assist in distinguishing tumor type and stage.

In the first study, the FMISO PET images were evaluated in different manners by visual assessment, SUV, lesion-to-normal tissue ratio, and uptake volume. The results of these analyses were consistent in showing the relationship between FMISO uptake and glioma grade. In clinical settings the findings suggest that a visual assessment is sufficient for a diagnosis, as the numerical values provide information consistent with the visual assessment. The numerical values may however be useful for purposes like assessing the prognosis and treatment response. Both the SUV_{max} and SUV_{10mm} with FMISO were higher in glioblastoma patients than in non-glioblastoma patients; the range of the values for the groups overlaps, possibly explained by inter-subject variability in the SUV. The lesion-to-cerebellum ratio clearly distinguished glioblastoma patients from non-glioblastoma patients. The usefulness of the lesion-to-cerebellum ratio has also been demonstrated by Bruehlmeier et al. [26], by showing that lesion-to-cerebellum ratios were comparable with the distribution of FMISO volumes. It may be argued that cerebral glioma patients often show asymmetric blood flows in the cerebellum (the so-called crossed cerebellar diaschisis) and that the cerebellar value may not be uniquely useful as a reference. In the study here, FMISO accumulation of the left and right cerebellar cortex did not show significant asymmetry (data not shown); however, this may be assumed not to be a problem in using the lesion-to-cerebellum ratio.

To further confirm the findings, the uptake volume of FMISO in the tumor was measured and compared for glioblastoma and non-glioblastoma patients. This comparison showed that glioblastomas exhibited significantly larger uptake volumes of FMISO than non-glioblastomas. In general, the hypoxic volume is distinguished with tissue-to-blood ratios ≥ 1.2 in images acquired 2 h after FMISO injection with venous blood samples [28–31]. In brain tumor segmentation for MET PET, a tumor-to-normal ratio ≥ 1.3 is frequently used [31, 39, 40, 48]. The study here did not collect blood samples at the scanning but showed intratumoral volumes in excess of a 1.3-fold cerebellum mean, which we consider an adequate substitute. The method here did not directly quantify the hypoxic volume, and this is one of the limitations of the study. As another limitation, the number of patients included in this study is small, and further study with more patients is necessary to substantiate the findings. In particular, such studies need to focus on small glioblastoma lesions and aggressive grade III tumors, because these could be a source of false-negative or positive results. Third, we did not investigate specific immunohistochemical features of hypoxia, like the hypoxia-inducible factor-1α (HIF-1α). Investigating HIF-1α further reveals the oxygen condition in the tumor. Finally, in clinical settings, metastatic brain tumors and malignant lymphomas also require a diagnosis that will distinguish them from glioblastomas. Further, additional and different types of brain tumors will need to be investigated.

We also wish to briefly discuss PET tracers other than FMISO [23]. The slow clearance of FMISO from tissue is a shortcoming in clinical settings. If the uptake time could be shortened to maybe 1 h, this would improve the feasibility of hypoxia imaging. Currently, FMISO is the tracer where most evidence has been accumulated, but promising data have been published for other tracers as well. A review article by Kurihara et al. on preclinical and clinical applications of hypoxia PET tracers including FMISO also mentions ^{18}F-fluoroerythronitroimidazole (FETNIM), ^{18}F-fluoroazomycin-arabinofuranoside (FAZA), and ^{62}Cu or ^{64}Cu-diacetyl-bis(N^4-methylthiosemicarbazone) (Cu-ATSM) [49]. Among these, FETNIM has not been used with brain tumors, while FAZA is less lipophilic than FMISO, suggesting that background activity in the plasma could be excreted more quickly than FMISO. This point is important for shortening the uptake time. However, in an animal study, Sorger et al. have showed that faster clearance of FAZA resulted in lower FAZA uptake in the tumor than with FMISO [50]. It is not easy to solve this dilemma between uptake time and contrast. Postema et al. conducted a study of FAZA PET in 50 patients with a number of different malignant tumors, including seven glioblastoma patients [51]. Here images were acquired 2–3 h after injection, and the image quality was reported as good, but not superior to FMISO. With Cu-ATSM there is the advantage that the radionuclide ^{62}Cu can be provided by a ^{62}Zn/^{62}Cu generator, which at present does not require an on-site cyclotron to image hypoxia. O'Donoghue et al. conducted an animal study using a R3327-AT tumor model and found a correlation between the 19-h images of Cu-ATSM and FMISO images at 2–4 h as well as oxygen probe measurements [52]. However, 1-h images of Cu-ATSM did not correlate with the FMISO images. A more recent study by Dence et al. compared Cu-ATSM with FMISO, FDG, and 18 F-fluorothymidine (FLT) using a 9 L gliosarcoma model. Here, autoradiography showed a strong correlation between the Cu-ATSM and FMISO distributions [53]. Tateishi et al. acquired Cu-ATSM PET for glioma patients and demonstrated a correlation between Cu-ATSM uptake and glioma grades [54]. Despite evidence, it is still not substantiated whether Cu-ATSM represents hypoxia. Further, ^{18}F-EF5, 2-(2-nitro-1[H]-imidazol-1-yl)-N-(2,2,3,3,3-pentafluoropropyl)-acetamide, was first tested in an animal study by Ziemer [55]. Evens et al. found that EF5 uptake correlated with a poor prognosis in glioma patients [18]. They also reported correlations of EF5 uptake with microscopic findings of vasculature [56] and radiation responses [57].

18.5 Conclusions

This article summarizes our recent findings in two studies related to FMISO PET for brain tumors. The first study demonstrated that much FMISO accumulated in glioblastomas but not in lower-grade gliomas. The second study demonstrated that FMISO PET images acquired 4 h after administration were better at showing hypoxic tumors than the images acquired 2 h after injection. Combining these

results, the 4-h FMISO PET may be useful in preoperatively discriminating glioblastomas from lower-grade gliomas.

References

1. Hirata K, Terasaka S, Shiga T, et al. (18)F-Fluoromisonidazole positron emission tomography may differentiate glioblastoma multiforme from less malignant gliomas. Eur J Nucl Med Mol Imaging. 2012;39:760–70.
2. Kobayashi K, Hirata K, Yamaguchi S, et al. FMISO PET at 4 hours showed a better lesion-to-background ratio uptake than 2 hours in brain tumors. J Nucl Med. 2015;56:S373.
3. Louis DN, Ohgaki H, Wiestler OD, et al. The 2007 WHO classification of tumours of the central nervous system. Acta Neuropathol. 2007;114:97–109.
4. Gorlia T, van den Bent MJ, Hegi ME, et al. Nomograms for predicting survival of patients with newly diagnosed glioblastoma: prognostic factor analysis of EORTC and NCIC trial 26981-22981/CE.3. Lancet Oncol. 2008;9:29–38.
5. Cho KH, Kim JY, Lee SH, et al. Simultaneous integrated boost intensity-modulated radiotherapy in patients with high-grade gliomas. Int J Radiat Oncol Biol Phys. 2010;78:390–7.
6. Behin A, Hoang-Xuan K, Carpentier AF, Delattre JY. Primary brain tumours in adults. Lancet. 2003;361:323–31.
7. Spetzler RF, Martin NA. A proposed grading system for arteriovenous malformations. J Neurosurg. 1986;65:476–83.
8. Brasch R, Pham C, Shames D, et al. Assessing tumor angiogenesis using macromolecular MR imaging contrast media. J Magn Reson Imaging. 1997;7:68–74.
9. Law M, Oh S, Babb JS, et al. Low-grade gliomas: dynamic susceptibility-weighted contrast-enhanced perfusion MR imaging--prediction of patient clinical response. Radiology. 2006;238:658–67.
10. Cao Y, Nagesh V, Hamstra D, et al. The extent and severity of vascular leakage as evidence of tumor aggressiveness in high-grade gliomas. Cancer Res. 2006;66:8912–7.
11. Emblem KE, Nedregaard B, Nome T, et al. Glioma grading by using histogram analysis of blood volume heterogeneity from MR-derived cerebral blood volume maps. Radiology. 2008;247:808–17.
12. Di Chiro G, DeLaPaz RL, Brooks RA, et al. Glucose utilization of cerebral gliomas measured by [18F] fluorodeoxyglucose and positron emission tomography. Neurology. 1982;32:1323–9.
13. Kaschten B, Stevenaert A, Sadzot B, et al. Preoperative evaluation of 54 gliomas by PET with fluorine-18-fluorodeoxyglucose and/or carbon-11-methionine. J Nucl Med. 1998;39:778–85.
14. Padma MV, Said S, Jacobs M, et al. Prediction of pathology and survival by FDG PET in gliomas. J Neurooncol. 2003;64:227–37.
15. Borbely K, Nyary I, Toth M, Ericson K, Gulyas B. Optimization of semi-quantification in metabolic PET studies with 18F-fluorodeoxyglucose and 11C-methionine in the determination of malignancy of gliomas. J Neurol Sci. 2006;246:85–94.

16. Oliver L, Olivier C, Marhuenda FB, Campone M, Vallette FM. Hypoxia and the malignant glioma microenvironment: regulation and implications for therapy. Curr Mol Pharmacol. 2009;2:263–84.
17. Flynn JR, Wang L, Gillespie DL, et al. Hypoxia-regulated protein expression, patient characteristics, and preoperative imaging as predictors of survival in adults with glioblastoma multiforme. Cancer. 2008;113:1032–42.
18. Evans SM, Judy KD, Dunphy I, et al. Hypoxia is important in the biology and aggression of human glial brain tumors. Clin Cancer Res. 2004;10:8177–84.
19. Lally BE, Rockwell S, Fischer DB, Collingridge DR, Piepmeier JM, Knisely JP. The interactions of polarographic measurements of oxygen tension and histological grade in human glioma. Cancer J. 2006;12:461–6.
20. Rasey JS, Grunbaum Z, Magee S, et al. Characterization of radiolabeled fluoromisonidazole as a probe for hypoxic cells. Radiat Res. 1987;111:292–304.
21. Martin GV, Caldwell JH, Rasey JS, Grunbaum Z, Cerqueira M, Krohn KA. Enhanced binding of the hypoxic cell marker [3H]fluoromisonidazole in ischemic myocardium. J Nucl Med. 1989;30:194–201.
22. Rasey JS, Koh WJ, Grierson JR, Grunbaum Z, Krohn KA. Radiolabelled fluoromisonidazole as an imaging agent for tumor hypoxia. Int J Radiat Oncol Biol Phys. 1989;17:985–91.
23. Kobayashi H, Hirata K, Yamaguchi S, Terasaka S, Shiga T, Houkin K. Usefulness of FMISO-PET for glioma analysis. Neurol Med Chir (Tokyo). 2013;53:773–8.
24. Valk PE, Mathis CA, Prados MD, Gilbert JC, Budinger TF. Hypoxia in human gliomas: demonstration by PET with fluorine-18-fluoromisonidazole. J Nucl Med. 1992;33:2133–7.
25. Rajendran JG, Mankoff DA, O'Sullivan F, et al. Hypoxia and glucose metabolism in malignant tumors: evaluation by [18F]fluoromisonidazole and [18F]fluorodeoxyglucose positron emission tomography imaging. Clin Cancer Res. 2004;10:2245–52.
26. Bruehlmeier M, Roelcke U, Schubiger PA, Ametamey SM. Assessment of hypoxia and perfusion in human brain tumors using PET with 18F-fluoromisonidazole and 15O-H2O. J Nucl Med. 2004;45:1851–9.
27. Cher LM, Murone C, Lawrentschuk N, et al. Correlation of hypoxic cell fraction and angiogenesis with glucose metabolic rate in gliomas using 18F-fluoromisonidazole, 18F-FDG PET, and immunohistochemical studies. J Nucl Med. 2006;47:410–8.
28. Spence AM, Muzi M, Swanson KR, et al. Regional hypoxia in glioblastoma multiforme quantified with [18F]fluoromisonidazole positron emission tomography before radiotherapy: correlation with time to progression and survival. Clin Cancer Res. 2008;14:2623–30.
29. Swanson KR, Chakraborty G, Wang CH, et al. Complementary but distinct roles for MRI and 18F-fluoromisonidazole PET in the assessment of human glioblastomas. J Nucl Med. 2009;50:36–44.
30. Szeto MD, Chakraborty G, Hadley J, et al. Quantitative metrics of net proliferation and invasion link biological aggressiveness assessed by MRI with hypoxia assessed by FMISO-PET in newly diagnosed glioblastomas. Cancer Res. 2009;69:4502–9.
31. Kawai N, Maeda Y, Kudomi N, et al. Correlation of biological aggressiveness assessed by 11C-methionine PET and hypoxic burden assessed by 18F-fluoromisonidazole PET in newly diagnosed glioblastoma. Eur J Nucl Med Mol Imaging. 2011;38:441–50.
32. Yamamoto Y, Maeda Y, Kawai N, et al. Hypoxia assessed by 18F-fluoromisonidazole positron emission tomography in newly diagnosed gliomas. Nucl Med Commun. 2012;33:621–5.
33. Grunbaum Z, Freauff SJ, Krohn KA, Wilbur DS, Magee S, Rasey JS. Synthesis and characterization of congeners of misonidazole for imaging hypoxia. J Nucl Med. 1987;28:68–75.
34. Thorwarth D, Eschmann SM, Paulsen F, Alber M. A kinetic model for dynamic [18F]-Fmiso PET data to analyse tumour hypoxia. Phys Med Biol. 2005;50:2209–24.
35. Oh SJ, Chi DY, Mosdzianowski C, et al. Fully automated synthesis of [18F]fluoromisonidazole using a conventional [18F]FDG module. Nucl Med Biol. 2005;32:899–905.
36. Tang G, Wang M, Tang X, Gan M, Luo L. Fully automated one-pot synthesis of [18F] fluoromisonidazole. Nucl Med Biol. 2005;32:553–8.

37. Minoshima S, Frey KA, Koeppe RA, Foster NL, Kuhl DE. A diagnostic approach in Alzheimer's disease using three-dimensional stereotactic surface projections of fluorine-18-FDG PET. J Nucl Med. 1995;36:1238–48.
38. Minoshima S, Koeppe RA, Frey KA, Kuhl DE. Anatomic standardization: linear scaling and nonlinear warping of functional brain images. J Nucl Med. 1994;35:1528–37.
39. Kracht LW, Miletic H, Busch S, et al. Delineation of brain tumor extent with [11C]L-methionine positron emission tomography: local comparison with stereotactic histopathology. Clin Cancer Res. 2004;10:7163–70.
40. Galldiks N, Ullrich R, Schroeter M, Fink GR, Jacobs AH, Kracht LW. Volumetry of [(11)C]-methionine PET uptake and MRI contrast enhancement in patients with recurrent glioblastoma multiforme. Eur J Nucl Med Mol Imaging. 2010;37:84–92.
41. Lee ST, Scott AM. Hypoxia positron emission tomography imaging with 18f-fluoromisonidazole. Semin Nucl Med. 2007;37:451–61.
42. Collingridge DR, Piepmeier JM, Rockwell S, Knisely JP. Polarographic measurements of oxygen tension in human glioma and surrounding peritumoural brain tissue. Radiother Oncol. 1999;53:127–31.
43. Koch CJ, Evans SM. Non-invasive PET and SPECT imaging of tissue hypoxia using isotopically labeled 2-nitroimidazoles. Adv Exp Med Biol. 2003;510:285–92.
44. Rasey JS, Nelson NJ, Chin L, Evans ML, Grunbaum Z. Characteristics of the binding of labeled fluoromisonidazole in cells in vitro. Radiat Res. 1990;122:301–8.
45. Kato T, Shinoda J, Oka N, et al. Analysis of 11C-methionine uptake in low-grade gliomas and correlation with proliferative activity. AJNR Am J Neuroradiol. 2008;29:1867–71.
46. Manabe O, Hattori N, Yamaguchi S, et al. Oligodendroglial component complicates the prediction of tumour grading with metabolic imaging. Eur J Nucl Med Mol Imaging. 2015;42:896–904.
47. Yamaguchi S, Terasaka S, Kobayashi H, et al. Combined use of positron emission tomography with (18)F-fluorodeoxyglucose and (11)C-methionine for preoperative evaluation of gliomas. No Shinkei Geka. 2010;38:621–8.
48. Kobayashi K, Hirata K, Yamaguchi S, et al. Prognostic value of volume-based measurements on (11)C-methionine PET in glioma patients. Eur J Nucl Med Mol Imaging. 2015;42:1071–80.
49. Kurihara H, Honda N, Kono Y, Arai Y. Radiolabelled agents for PET imaging of tumor hypoxia. Curr Med Chem. 2012;19:3282–9.
50. Sorger D, Patt M, Kumar P, et al. [18F]Fluoroazomycinarabinofuranoside (18FAZA) and [18F]Fluoromisonidazole (18FMISO): a comparative study of their selective uptake in hypoxic cells and PET imaging in experimental rat tumors. Nucl Med Biol. 2003;30:317–26.
51. Postema EJ, McEwan AJ, Riauka TA, et al. Initial results of hypoxia imaging using 1-alpha-D: −(5-deoxy-5-[18F]-fluoroarabinofuranosyl)-2-nitroimidazole (18F-FAZA). Eur J Nucl Med Mol Imaging. 2009;36:1565–73.
52. O'Donoghue JA, Zanzonico P, Pugachev A, et al. Assessment of regional tumor hypoxia using 18F-fluoromisonidazole and 64Cu(II)-diacetyl-bis(N4-methylthiosemicarbazone) positron emission tomography: Comparative study featuring microPET imaging, Po2 probe measurement, autoradiography, and fluorescent microscopy in the R3327-AT and FaDu rat tumor models. Int J Radiat Oncol Biol Phys. 2005;61:1493–502.
53. Dence CS, Ponde DE, Welch MJ, Lewis JS. Autoradiographic and small-animal PET comparisons between (18)F-FMISO, (18)F-FDG, (18)F-FLT and the hypoxic selective (64)Cu-ATSM in a rodent model of cancer. Nucl Med Biol. 2008;35:713–20.
54. Tateishi K, Tateishi U, Sato M, et al. Application of 62Cu-diacetyl-bis (N4-methylthiosemicarbazone) PET imaging to predict highly malignant tumor grades and hypoxia-inducible factor-1alpha expression in patients with glioma. AJNR Am J Neuroradiol. 2013;34:92–9.
55. Ziemer LS, Evans SM, Kachur AV, et al. Noninvasive imaging of tumor hypoxia in rats using the 2-nitroimidazole 18F-EF5. Eur J Nucl Med Mol Imaging. 2003;30:259–66.
56. Evans SM, Jenkins KW, Jenkins WT, et al. Imaging and analytical methods as applied to the evaluation of vasculature and hypoxia in human brain tumors. Radiat Res. 2008;170:677–90.
57. Koch CJ, Shuman AL, Jenkins WT, et al. The radiation response of cells from 9L gliosarcoma tumours is correlated with [F18]-EF5 uptake. Int J Radiat Biol. 2009;85:1137–47.

Chapter 19
Evolution and Protection of Cerebral Infarction Evaluated by PET and SPECT

Eku Shimosegawa

Abstract Since cerebral infarction results from a reduction of cerebral blood flow (CBF) by the occlusion or stenosis of carotid or intracranial arteries, CBF is a primary parameter to predict of ischemic brain injury. Single-photon emission tomography (SPECT) and positron emission tomography (PET) contributed to evaluate loss of cerebral autoregulation, uncoupling state between CBF and brain metabolism, and ischemic penumbra. Measurement of CBF and oxygen metabolism by ^{15}O PET revealed the process of infarct growth in hyperacute stage of cerebral infarction and areas with depressed oxygen metabolism, but normal water diffusion in magnetic resonance imaging (MRI) was termed as "metabolic penumbra." Recently, some researchers shed light on the role of glial cells in the energy metabolism of the brain and ^{11}C-acetate PET and demonstrated that astrocytic energy metabolism in TCA cycle was protective against ischemia. SPECT and PET studies for secondary reaction after ischemia (i.e., selective neuronal loss by ^{123}I-iomazenil SPECT and ^{11}C-flumazenil PET, tissue hypoxia by ^{18}F-FMISO PET, and neuroinflammation by TSPO-PET) are expected as new biomarkers. Combining these imaging biomarkers with classical CBF measurement may contribute to develop innovative drugs for pharmacological neuroprotection in the therapy of cerebral infarction.

Keywords Cerebral infarction • SPECT • PET • Hypoxia • TSPO-PET

19.1 Introduction

Cerebral infarction results from a reduction in cerebral blood flow (CBF) arising from the occlusion or stenosis of carotid or intracranial arteries, and the progression of this event typically ends with the necrosis of various brain tissue components, including neurons. Since tissue damage varies according to the severity of brain

E. Shimosegawa, MD, PhD (✉)
Department of Molecular Imaging in Medicine, Graduate School of Medicine, Osaka University, 2-2 Yamadaoka, Suita, Osaka 565-0871, Japan
e-mail: eku@mi.med.osaka-u.ac.jp

Y. Kuge et al. (eds.), *Perspectives on Nuclear Medicine for Molecular Diagnosis and Integrated Therapy*, DOI 10.1007/978-4-431-55894-1_19

ischemia, CBF is a primary parameter for predicting the extent of ischemic brain injury.

Positron emission tomography (PET) and single-photon emission computed tomography (SPECT) have contributed to the elucidation of the disease process responsible for brain ischemia from an acute to chronic stage. PET studies have mainly measured CBF and oxygen metabolism but have been expanded to include the detection of neuronal loss, tissue hypoxia, and neuroinflammation. Quantitative ^{15}O PET measurements can provide information on CBF, the cerebral metabolic rate of oxygen ($CMRO_2$), the cerebral blood volume (CBV), and the oxygen extraction fraction (OEF), and these parameters enable impaired cerebral autoregulation and the uncoupling of perfusion and metabolism to be diagnosed based on absolute values. The SPECT studies can visualize the magnitude and extent of ischemia in a clinical setting. Neurons are more vulnerable than other cell groups in the brain, and selective neuronal loss sometimes occurs in patients with mild to moderate brain ischemia. PET and SPECT are advantageous for demonstrating this type of brain injury, which cannot be visualized by comparing computed tomography (CT) and magnetic resonance imaging (MRI) findings. PET imaging of tissue hypoxia is expected to distinguish permanent and temporal ischemic areas surrounding the ischemic core. Translocator protein (TSPO) PET can represent neuroinflammation in areas with evolving infarcts and may become a biomarker for neuroprotective therapy. Recently, important roles of astrocytes in the energy metabolism of the brain have been reported. The imaging of astrocytes using ^{11}C-acetate PET may provide a sensitive marker for evaluating glial metabolism in the ischemic brain. The purpose of using these imaging probes depends on the course or stage of

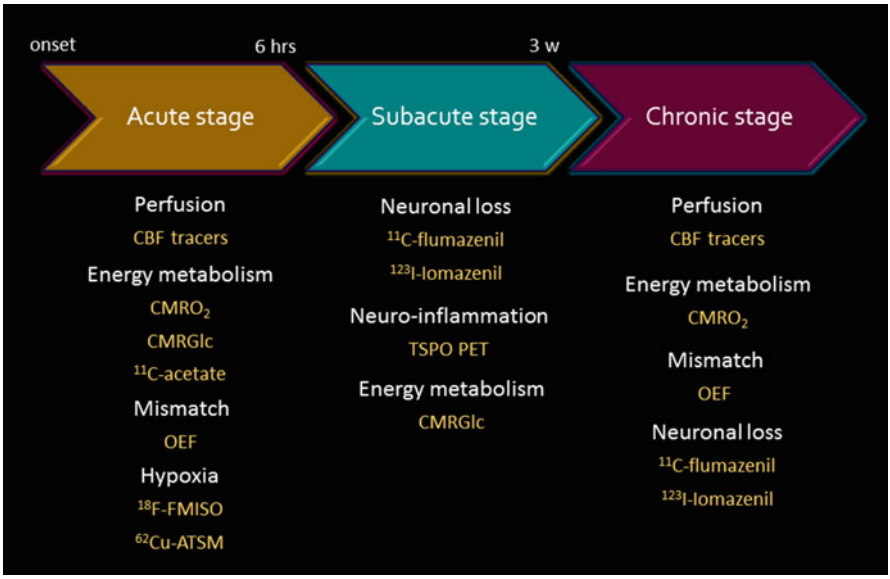

Fig. 19.1 Time course of infarct evolution and related PET/SPECT imaging

cerebral infarction (Fig. 19.1). In this chapter, we introduce the use of PET and SPECT imaging in studies to clarify the process of cerebral infarction.

19.2 Perfusion and Oxygen Metabolism in Brain Ischemia

CBF is a key parameter of ischemic brain damage that can be quantitatively measured using PET and SPECT. A decrease in the cerebral perfusion pressure (CPP) induces primary damage to the supply of oxygen and energy substance to the brain. Protective mechanisms against reductions in the CPP can be evaluated using PET and SPECT. The first mechanism is "cerebral autoregulation," the origin of which is cardiac pump function. CBF is constant within a mean arterial blood pressure (MABP) range of 60–160 mmHg [1]. To maintain a constant CBF, cerebral precapillary arterioles can dilate when the CPP decreases and can constrict when the CPP increases. Although this mechanism of dilation and constriction for cerebral autoregulation remains unclear, recent studies have indicated that CBF control is initiated in the cerebral capillaries, where pericytes can constrict capillaries in response to the effect of noradrenaline [2]. Cerebral autoregulation is disturbed by brain ischemia [3], and its capacity can be estimated using the cerebral vasoreactivity (CVR) to the change in the arterial partial pressure of carbon dioxide ($PaCO_2$). In SPECT studies, acetazolamide, which is another vasodilating agent, is used to test CVR. A reduced CVR in patients with steno-occlusive carotid artery disease is a major predictor of stroke recurrence [4, 5].

By combining this information with data on CBF and oxygen metabolism measured using ^{15}O PET, we can evaluate other protective states against CPP reduction (Fig. 19.2). When cerebral autoregulation is functioning well, CBF remains normal and the CBV increases, indicating the dilatation of collateral vessels. When the CPP is reduced beyond the point of compensation by vasodilatation, the cerebral autoregulation is exhausted and the CBF begins to decrease.

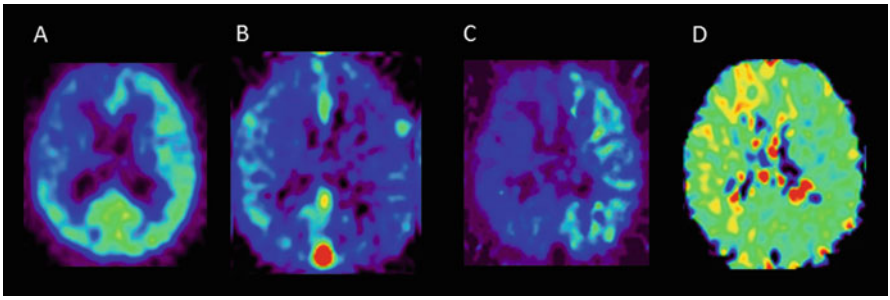

Fig. 19.2 ^{15}O PET images in a patient with right carotid and MCA occlusion. PET images of (**a**) CBF, (**b**) CBV, (**c**) CPP, and (**d**) OEF. The CPP images were created by dividing CBF and CBV. The area with a severe CPP reduction corresponded to the area with an elevated OEF (misery perfusion)

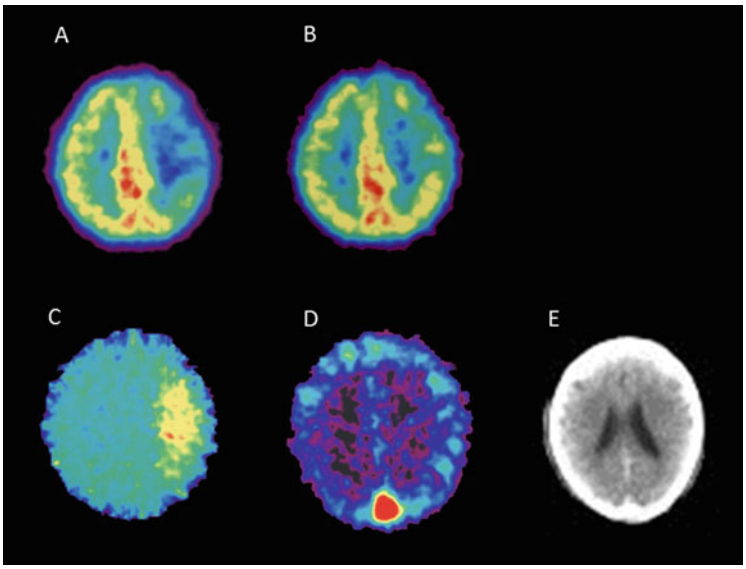

Fig. 19.3 Misery perfusion in a patient with acute left MCA occlusion. PET images of (**a**) CBF, (**b**) $CMRO_2$, (**c**) OEF, and (**d**) CBV examined on the day of stroke onset. The CBF in the left MCA territory reduced, whereas the $CMRO_2$ in the corresponding area was relatively preserved. The OEF was elevated in the same area, indicating an uncoupled state between perfusion and oxygen metabolism (misery perfusion). A CT image obtained on the same day (**e**) did not show any morphological changes

When $CMRO_2$ is preserved, then the OEF starts to increase. Such increases in the OEF are known as "misery perfusion" and can be observed during the acute stage of cerebral infarction (Fig. 19.3). In the chronic stage of cerebral infarction, misery perfusion in patients with unilateral carotid artery occlusion suggests a high probability of stroke recurrence [6–8]. Powers et al. classified the severity of cerebral ischemia from Stage 0 to Stage II according to CBF, CBV, and OEF [9]. Stage II is equal to the state of misery perfusion. The 5-year stroke recurrence rate for Stage II patients with unilateral steno-occlusive internal carotid artery (ICA) was 70 %, whereas it was 20 % for Stage 0 and I patients [8].

19.3 Infarct Growth in Acute Cerebral Infarction

The ischemic threshold of CBF has been thoroughly evaluated in both experimental studies and clinical studies. Symon and colleagues revealed a relationship between CBF, neurological deficits, and tissue damage in baboon models of cerebral ischemia [10]. They showed that the electric activity of somatosensory evoked potentials in cerebral tissue was preserved at a CBF above 20 mL/100 g/min (40 % of normal level), whereas it was impaired when the CBF decreased to 10–20 mL/100 g/min.

Although this impaired electric activity was reversible by recirculation, irreversible damage resulting from an elevated extracellular potassium concentration and subsequent cell death occurred when the CBF was reduced to less than 6–10 mL/100 g/min. Astrup, Siesjo, and Symon defined the ischemic penumbra as brain tissue with CBF thresholds between electric (20 mL/100 g/min) and membrane failure (6–10 mL/100 g/min) [11]. In a baboon model, Jones et al. found that a longer period of ischemia was associated with a higher threshold for membrane failure [12]. Their studies indicated that the ischemic penumbra should be restored as early as possible to reduce the volume of cerebral infarction. Clinical SPECT studies have demonstrated the validity of evaluating the ischemic threshold during the acute stage of infarction. Shimosegawa et al. evaluated SPECT images within 6 h of onset in ischemic stroke patients and revealed that a CBF of less than 30–50 % of that in unaffected brain regions was capable of inducing cerebral infarction [13] (Fig. 19.4). When the CBF was less than 20 % of that in the unaffected hemisphere, the probability of hemorrhagic infarction after recanalization therapy increased [14].

Although the CBF threshold has been established in both experimental and clinical studies, the metabolic threshold and its relation to the development of infarction has not yet been clarified. In a ^{15}O PET study of patients with cerebral infarction where imaging was performed within 6 h of onset, Shimosegawa et al. demonstrated that infarct growth occurred in brain lesions with a depressed $CMRO_2$ but normal water diffusion on diffusion-weighted imaging (DWI) [15] (Fig. 19.5). Peri-infarct areas with a $CMRO_2$ of less than 45–62 % of that in unaffected brain regions on the initial ^{15}O PET showed volume expansion of the brain infarction at 3 days after onset, and they named this phenomenon "metabolic penumbra." The normal diffusion in these areas indicated that adenosine triphosphate (ATP) synthesis was still preserved to a degree sufficient to maintain an

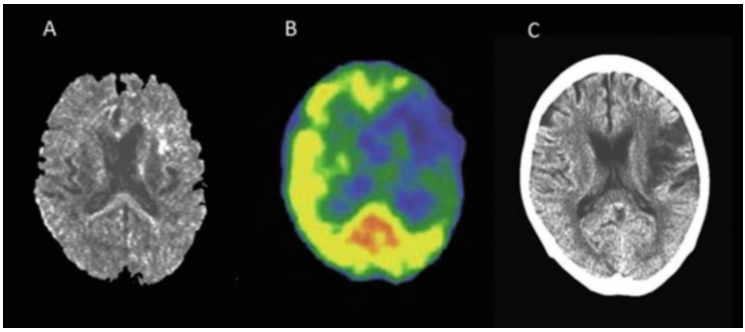

Fig. 19.4 Prediction of cerebral infarction by acute CBF-SPECT. A diffusion-weighted MR image obtained at 1.3 h after onset (**a**) demonstrated only a small lesion in the frontal lobe. A ^{99m}HMPAO-SPECT image obtained at 2.3 h after onset (**b**) showed a broad reduction in CBF in the left cerebral hemisphere. A CBF reduction of more than 50 %, compared with the contralateral region, was observed in the left frontal lobe, and this area progressed into a complete infarction visible on a CT image obtained 4 days after onset (**c**)

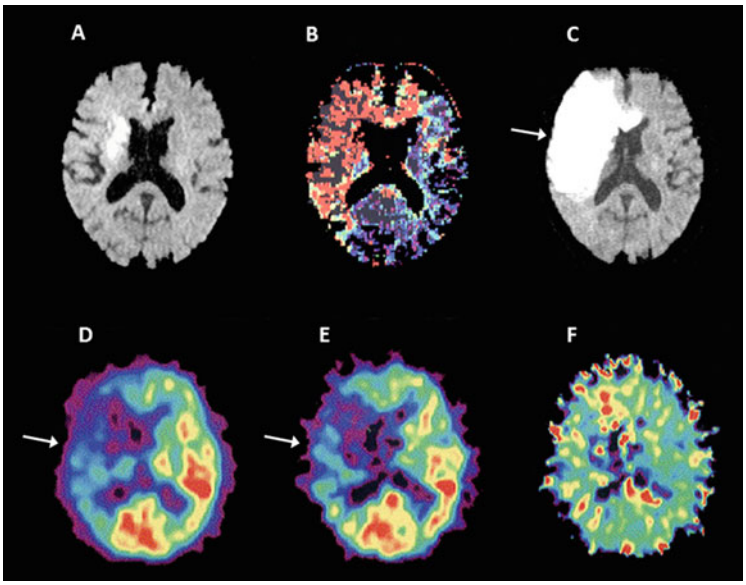

Fig. 19.5 Metabolic penumbra in acute brain infarction. (**a**) DWI of MRI obtained 4 h after onset, (**b**) perfusion-weighted image (PWI) obtained 4 h after onset, (**c**) DWI obtained 3 days after onset, (**d**) CBF obtained 3 h after onset, (**e**) $CMRO_2$ obtained 3 h after onset, and (**f**) OEF obtained 3 h of onset in a patient with right ICA embolic occlusion. An MRI examination indicated PWI–DWI mismatch in the territory of the right ICA. DWI on day 3 indicated an evolution of the infarction within the mismatch. The initial PET examination indicated that the PWI–DWI mismatch lesion exhibited reductions in CBF and $CMRO_2$ associated with misery perfusion (increased OEF, *white arrow*). The PWI–DWI mismatch corresponded to suppressed energy metabolism that was still higher than the threshold for ion pump failure (Reprinted from Brain Mapping: An Encyclopedic Reference, Vol. 3/1st edition, Arthur W. Toga (Editor in Chief), Hemodynamic and Metabolic Disturbances in Acute Cerebral Infarction (title)/Clinical Brain Mapping (chapter), written by E. Shimosegawa, p. 829–838, 2015, with permission from Elsevier)

ATP-dependent neuronal membrane ion pump in the area of the evolving infarct as early as 6 h after onset. Therefore, a metabolic penumbra with a moderate decrease in $CMRO_2$ would be a critical treatment target, using early reperfusion and pharmacological neuroprotection to reduce the volume expansion of the brain infarction.

19.4 Role of Astrocytic Function in Brain Ischemia

Recently, some researchers have shed light on the role of glial cells in energy metabolism in the brain. Glutamate is a major excitatory neurotransmitter of the brain, and glutamate in the synaptic cleft is removed by astrocytes surrounding glutaminergic synapses. The removed glutamate is converted into glutamine in astrocytes by glutamine synthetase. Glutamine is released by astrocytes and taken

up by neuronal terminals, where it is enzymatically reconverted to glutamate and stored in the neurotransmitter pool for the next transmission. This process is called "glutamate-glutamine cycle" and requires ATP [16]. Furthermore, astrocytes play an important role in glycolysis in the brain. Activation by the glutamate transporter on the astrocytic membrane stimulates glucose uptake into astrocytes. This glucose is processed glycolytically, resulting in the release of lactate as an energy substrate for neurons. Lactate produced by this process is transferred to neurons for oxidation (the astrocyte-neuron lactate shuttle: ANLS) [17]. This lactate produces two ATP molecules, which contribute to the Na-K ion pump function and the synthesis of glutamine from glutamate. In ischemic brain where ATP synthesis is restricted, the conversion of glutamate in the synaptic cleft is disturbed. Continuous stimulation by glutamate induces an influx of Ca^{2+} ion, resulting in anoxic depolarization, and leads to inflammation and apoptosis. Therefore, the glutamate-glutamine cycle and ANLS are deeply related to astrocytic function and plays a critical role in the evolution from penumbra to infarction.

For the specific imaging of astrocyte, acetate is expected to be useful as a selective marker of astrocytic energy metabolism [18, 19]. ^{14}C-acetate is rapidly incorporated into glutamine via glutamate by glutamine synthetase localized in astrocytic cells [20]. Hosoi et al. demonstrated that ^{14}C-acetate uptake is dramatically decreased in a 3-min ischemia and reperfusion model, indicating that the metabolic and functional impairment of astrocytes continues after the restoration of CBF [21]. ^{11}C-labeled acetate could be a promising PET tracer for the evaluation of astrocytic metabolism in human studies (Fig. 19.6).

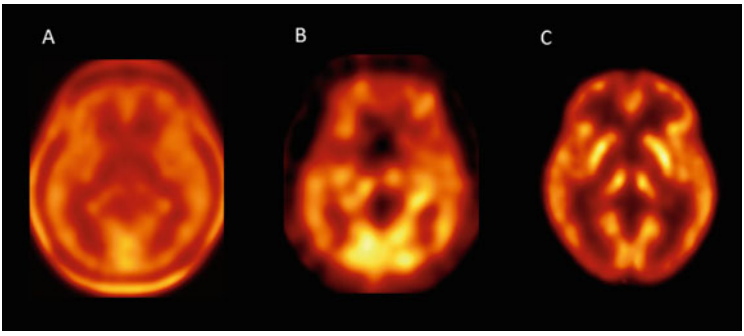

Fig. 19.6 Qualitative and quantitative ^{11}C-acetate PET imaging for astrocytic energy metabolism. (**a**) An averaged ^{11}C-acetate PET image (from 0 to 40 min) and (**b**) an averaged Kmono image in a healthy volunteer. The energy metabolism evaluated using the Kmono image was different from the normal oxygen metabolism evaluated using the $CMRO_2$ image (**c**)

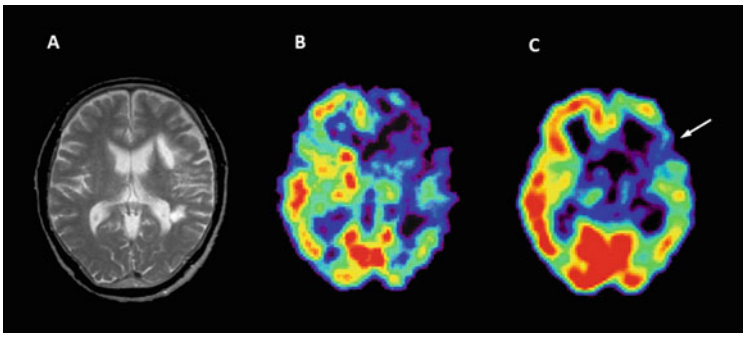

Fig. 19.7 Selective neuronal loss: (**a**) T_2-weighted image (T_2WI) in a patient with subcortical infarction of the left putamen 1.5 months after onset, (**b**) CBF image of the corresponding slice obtained by ^{123}I-IMP SPECT, and (**c**) ^{123}I-iomazenil SPECT image of the corresponding slice. The MR image showed no obvious lesion in the left cortical area, whereas ^{123}I-iomazenil SPECT demonstrated a decrease in accumulation (*white arrow*), indicating selective neuronal loss. The CBF reduction extended beyond the cortical areas of ^{123}I-iomazenil reduction (Reprinted from Brain Mapping: An Encyclopedic Reference, Vol. 3/1st edition, Arthur W. Toga (Editor in Chief), Hemodynamic and Metabolic Disturbances in Acute Cerebral Infarction (title)/Clinical Brain Mapping (chapter), written by E. Shimosegawa, p. 829–838, 2015, with permission from Elsevier)

19.5 Selective Neuronal Loss in Ischemic Brain Injury

Tissue vulnerability differs among neurons, glial cells, and blood vessels. Selective neuronal necrosis is known to occur in neuron-specific ischemic injury, where other cell components are preserved, and is associated with the expression of apoptosis-related DNA damages and repair genes [22]. In PET and SPECT imaging, ^{11}C-flumazenil and ^{123}I-iomazenil are considered to be neuron-specific tracers that bind central benzodiazepine receptors that are specifically localized on the membranes of cortical neurons. Preserved ^{11}C-flumazenil accumulation in acute ischemic brain can predict the probability of surviving an infarct [23, 24]. Hatazawa et al. examined ^{123}I-iomazenil SPECT in patients with cortical and subcortical infarction. They reported a patient with global aphasia who had a purely subcortical infarction and significantly diminished ^{123}I-iomazenil uptake in CT-negative Broca and Wernicke areas [25]. This result indicated that ^{123}I-iomazenil SPECT could sensitively detect lesions responsible for clinical symptoms, compared with morphological examinations (Fig. 19.7).

19.6 Detection of Tissue Hypoxia

Tissue hypoxia can be visualized using ^{18}F-labeled nitroimidazole derivatives or $^{62/64}$Cu-labeled lipophilic chelate compounds. ^{18}F-fluoromisonidazole (^{18}F-FMISO) PET is a representative hypoxic marker. Under hypoxic conditions, ^{18}F-FMISO

passively diffuses into cells and is reduced by nitroreductase enzymes and trapped by intracellular molecules. The retention of ^{18}F-FMISO is inversely proportional to the tissue partial pressure of O_2. Takasawa et al. revealed that the selective accumulation of ^{18}F-FMISO was found in permanent and temporal ischemic areas surrounding the ischemic core [26]. They demonstrated that ^{18}F-FMISO uptake in the ischemic brain was only elevated during the early phase of middle cerebral artery (MCA) occlusion. After early reperfusion, no demonstrable tracer retention was observed. In patients with an acute MCA territory stroke, Markus et al. reported that ^{18}F-FMISO PET showed the temporal evolution of tissue hypoxia [27]. A higher hypoxic volume was observed in the core of the infarct within 6 h of onset, and the location moved to the periphery or external to the infarct at later time points. They also showed that tissue without ^{18}F-FMISO uptake within the final infarct was presumed to have infarcted by the time of the acute ^{18}F-FMISO PET. These experimental and clinical results are very interesting because they suggested that ^{18}F-FMISO uptake changes continuously during the course of brain infarction. Since ^{18}F-FMISO PET is unable to discriminate between complete infarcted area and non-hypoxic viable tissue during the acute stage of infarction, the timing of the PET examination is likely to be critical for diagnosing whether the tissue is salvageable.

19.7 Imaging of Neuroinflammation

In focal brain ischemia, inflammatory reactions mainly occur in the peri-infarct area and lead to an overexpression of peripheral benzodiazepine receptors (PBR)/18-kDa TSPO on the membrane of activated microglia, macrophages, and activated astrocytes. Several PET tracers that specifically bind to TSPO have been developed as biomarkers of neuroinflammation. Imaizumi et al. demonstrated that ^{11}C-PBR28 accumulated in the peri-infarct lesions of a rat ischemia model, indicating that neuroinflammation does not occur in the ischemic core but in penumbral lesions [28]. In our preclinical study using a temporary MCA occlusion model, ^{11}C-DPA-713 uptake increased in the area surrounding the infarct core after 4 days of ischemia, where the expression of microglia/macrophages was positive using CD11b immunostaining (Fig. 19.8). In an impressive study, Martín et al. reported that ^{18}F-DPA-714 uptake decreased at 7 days after cerebral ischemia in rats treated with minocycline, compared with saline-treated animals [29]. Whether the increased regional microglia/macrophage activation visualized by TSPO PET is a good biomarker remains controversial. TSPO molecular imaging, however, might have diagnostic potential for assessing therapeutic strategies, such as the use of neuroprotective or anti-inflammatory drugs during the acute or subacute stage of cerebral infarction.

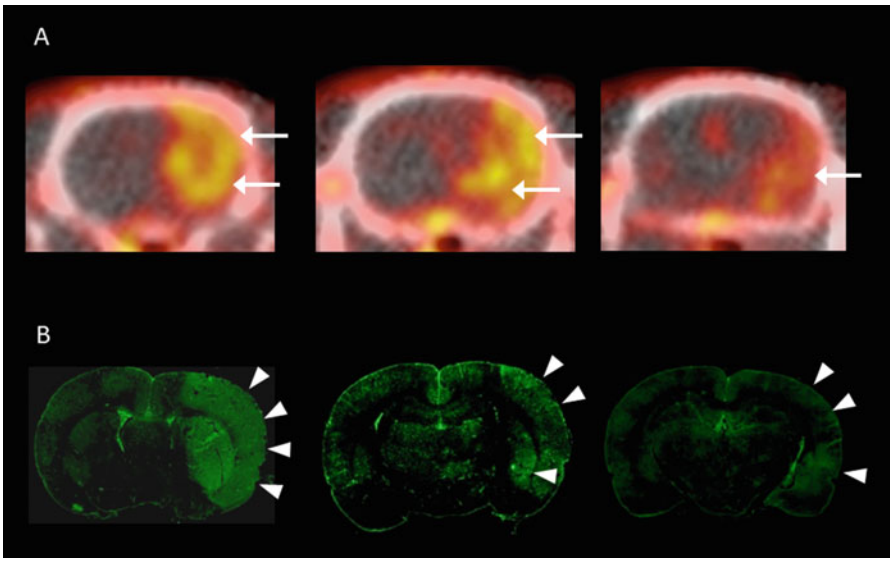

Fig. 19.8 TSPO PET image of rat ischemic model. (**a**) ^{11}C-DPA713 PET and (**b**) the corresponding CD11b immunostaining image. ^{11}C-DPA713 accumulated in the peripheral region of the ischemic core at 4 days after 60 min of MCA occlusion and reperfusion (*white arrows*). The CD11b-positive findings agreed with the uptake of ^{11}C-DPA713 (*white arrow* heads), indicating that macrophages/microglia were activated by neuroinflammation after brain ischemia

19.8 Summary

Measurements of hemodynamic and metabolic disturbances using PET and SPECT have been utilized to study the acute and chronic stages of cerebral infarction. CBF, $CMRO_2$, CBV, OEF, and CVR are basic parameters for estimating CPP reduction. An acute metabolic penumbra (decreased $CMRO_2$ in peri-infarct area on initial PET) and misery perfusion (areas with decreased CBF with maintained $CMRO_2$ in ischemic brain) during the acute and chronic stages are indicators of evolving infarction. Astrocytes have a protective role against cerebral infarction by reducing the glutamate concentration during ischemia, and ^{11}C-acetate PET may provide information regarding glial cell function. Neuron-specific imaging can only be performed using PET and SPECT, and it would be useful to collate the clinical symptoms with neuronal damage. PET tracers for tissue hypoxia and neuroinflammation have been developed and are promising biomarkers for detecting infarct growth and salvageable tissue and are expected to become useful as probes in future therapeutic interventions.

References

1. Paulson OB, Strandgaard S, Edvinsson L. Cerebral autoregulation. Cerebrovasc Brain Metab Rev. 1990;2:161–92.
2. Peppiatt CM, Howarth C, Mobbs P, Attwell D. Bidirectional control of CNS capillary diameter by pericytes. Nature. 2006;443:700–4.
3. Lassen NA. The luxury perfusion syndrome and its possible relation to acute metabolic acidosis localized within the brain. Lancet. 1966;2:1113–5.
4. Kuroda S, Houkin K, Kamiyama H, Mitsumori K, Iwasaki Y, Abe H. Long-term prognosis of medically treated patients with internal carotid or middle cerebral artery occlusion: can acetazolamide test predict it? Stroke. 2001;32:2110–6.
5. Ogasawara K, Ogawa A, Yoshimoto T. Cerebrovascular reactivity to acetazolamide and outcome in patients with symptomatic internal carotid or middle cerebral artery occlusion: a xenon-133 single-photon emission computed tomography study. Stroke. 2002;33:1857–62.
6. Yamauchi H, Fukuyama H, Nagahama Y, Nabatame H, Nakamura K, Yamamoto Y, et al. Evidence of misery perfusion and risk for recurrent stroke in major cerebral arterial occlusive diseases from PET. J Neurol Neurosurg Psychiatry. 1996;61:18–25.
7. Grubb Jr RL, Derdeyn CP, Fritsch SM, Carpenter DA, Yundt KD, Videen TO, et al. Importance of hemodynamic factors in the prognosis of symptomatic carotid occlusion. JAMA. 1998;280:1055–60.
8. Yamauchi H, Fukuyama H, Nagahama Y, Nabatame H, Ueno M, Nishizawa S, et al. Significance of increased oxygen extraction fraction in five-year prognosis of major cerebral arterial occlusive diseases. J Nucl Med. 1999;40:1992–8.
9. Powers WJ, Grubb Jr RL, Raichle ME. Physiological responses to focal cerebral ischemia in humans. Ann Neurol. 1984;16:546–52.
10. Symon L, Pasztor E, Branston NM. The distribution and density of reduced cerebral blood flow following acute middle cerebral artery occlusion: an experimental study by the technique of hydrogen clearance in baboons. Stroke. 1975;6:476–81.
11. Astrup J, Siesjo BK, Symon L. Thresholds in cerebral ischemia- the ischemic penumbra. Stroke. 1981;12:723–5.
12. Jones TH, Morawetz RB, Crowell RM, Marcoux FW, FitzGibbon SJ, DeGirolami U, et al. Thresholds of focal cerebral ischemia in awake monkeys. J Neurosurg. 1981;54:583–5.
13. Shimosegawa E, Hatazawa J, Inugami A, Fujita H, Ogawa T, Aizawa Y, et al. Cerebral infarction within six hours of onset: prediction of complete infarction with technetium-99m-HMPAO SPECT. J Nucl Med. 1994;35:1097–103.
14. Ueda T, Hatakeyama T, Kumon Y, Sasaki S, Uraoka T. Evaluation of risk of hemorrhagic transformation in local intra-arterial thrombolysis in acute ischemic stroke by initial SPECT. Stroke. 1994;25:298–303.
15. Shimosegawa E, Hatazawa J, Ibaraki M, Toyoshima H, Suzuki A. Metabolic penumbra in acute brain infarction: a correlation with infarct growth. Ann Neurol. 2005;57:495–504.

16. Dienel GA, Cruz NF. Astrocyte activation in working brain: energy supplied by minor substrates. Neurochem Int. 2006;48:568–95.
17. Pellerin L, Magistretti P. Sweet sixteen for ANLS. J Cereb Blood Flow Metab. 2012;32:1152–66.
18. Muir D, Berl S, Clarke DD. Acetate and fluoroacetate as possible markers for glial metabolism in vivo. Brain Res. 1986;380:336–40.
19. Cerdan S, Kunnecke B, Seelig J. Cerebral metabolism of [1,2-^{13}C2]acetate as detected by *in vivo* and *in vitro* ^{13}C NMR. J Biol Chem. 1990;265:12916–26.
20. Martinez Hernandez A, Bell KP, Norenberg MD. Glutamine synthetase: glial localization in brain. Science. 1977;195:1356–8.
21. Hosoi R, Kashiwagi Y, Tokumura M, Abe K, Hatazawa J, Inoue O. Sensitive reduction in 14C-acetate uptake in a short-term ischemic rat brain. J Stroke Cerebrovasc Dis. 2007;16:77–81.
22. Nedergaard M. Neuronal injury in the infarct border: a neuropathological study in the rat. Acta Neuropath (Berl). 1987;73:267–74.
23. Heiss WD, Kracht LW, Thiel A, Grond M, Pawlik G. Penumbral probability thresholds of cortical flumazenil binding and blood flow predicting tissue outcome in patients with cerebral ischaemia. Brain. 2001;124:20–9.
24. Guadagno JV, Jones PS, Aigbirhio FI, Wang D, Fryer TD, Day DJ, et al. Selective neuronal loss in rescued penumbra relates to initial hypoperfusion. Brain. 2008;131:2666–78.
25. Hatazawa J, Satoh T, Shimosegawa E, Okudera T, Inugami A, Ogawa T, et al. Evaluation of cerebral infarction with iodine 123-iomazenil SPECT. J Nucl Med. 1995;36:2154–61.
26. Takasawa M, Beech JS, Fryer TD, Hong YT, Hughes JL, Igase K, et al. Imaging of brain hypoxia in permanent and temporary middle cerebral artery occlusion in the rat using ^{18}F-fluoromisonidazole and positron emission tomography: a pilot study. J Cereb Blood Flow Metab. 2007;27:679–89.
27. Markus R, Reutens DC, Kazui S, Read S, Wright P, Chambers BR, et al. Topography and temporal evolution of hypoxic viable tissue identified by ^{18}F-fluoromisonidazole positron emission tomography in humans after ischemic stroke. Stroke. 2003;34:2646–52.
28. Imaizumi M, Kim HJ, Zoghbi SS, Briard E, Hong J, Musachio JL, et al. PET imaging with [11C]PBR28 can localize and quantify upregulated peripheral benzodiazepine receptors associated with cerebral ischemia in rat. Neurosci Lett. 2007;411:200–5.
29. Martín A, Boisgard R, Kassiou M, Dollé F, Tavitian B. Reduced PBR/TSPO expression after minocycline treatment in a rat model of focal cerebral ischemia: a PET study using [^{18}F]DPA-714. Mol Imaging Biol. 2010;13:10–5.

Chapter 20
Brain Development and Aging Using Large Brain MRI Database

Yasuyuki Taki

Abstract Now we confront a super aging society in Japan. In the situation, it is important to preserve our cognitive function for entire life by preventing us from pathological brain aging. To perform the aim, we have built a large brain magnetic resonance imaging (MRI) database from around 3,000 subjects aged from 5 to 80 in order to reveal how brain develops and ages. We have also collected several cognitive functions, lifestyle such as eating and sleeping habits, and genetic data. Using the database, we have revealed normal brain development and aging and also have revealed what factors affect brain development and aging. For example, sleep duration is significantly associated with the gray matter volume of the bilateral hippocampi. In addition, there were significant negative correlation between alcohol drinking and gray matter volume of the frontoparietal region and body mass index and gray matter volume of the hippocampus in cross-sectional analysis. In addition, having intellectual curiosity showed significant negative correlation with regional gray matter volume decline rate in the temporoparietal region. These findings help understanding the mechanism of brain development and aging as well as performing differential diagnosis or diagnosis at an early stage of several diseases/disorders such as autism and Alzheimer's disease.

Keywords Brain development • Brain aging • Magnetic resonance imaging • Database • Preventive medicine • Normal subject

Y. Taki (✉)
Department of Nuclear Medicine & Radiology, Institute of Development, Aging and Cancer, Tohoku University, 4-1 Seiryo-cho, Aoba-ku, 980-8575 Sendai, Japan

Division of Medical Neuroimage Analysis, Department of Community Medical Supports, Tohoku Medical Megabank Organization, Tohoku University, 4-1 Seiryo-cho, Aoba-ku, 980-8575 Sendai, Japan

Division of Developmental Cognitive Neuroscience, Institute of Development, Aging and Cancer, Tohoku University, 4-1 Seiryo-cho, Aoba-ku, 980-8575 Sendai, Japan
e-mail: ytaki@idac.tohoku.ac.jp

Y. Kuge et al. (eds.), *Perspectives on Nuclear Medicine for Molecular Diagnosis and Integrated Therapy*, DOI 10.1007/978-4-431-55894-1_20

20.1 Introduction

Now we confront a super aging society in Japan. In the situation, it is important to preserve our cognitive function for entire life by preventing us from pathological brain aging. Recently, the importance of human neuroimaging database was recognized greatly. The normal brain structure and function database can be used as the references not only for neuroimaging study for humans but also for early diagnosis and computer-aided automated diagnosis of the brain diseases. The most remarkable recently developed method for brain image analysis is voxel-based morphometry (VBM). It includes anatomical standardization of the brain to a standard brain, brain tissue segmentation and finally voxel-based statistical analysis based on general linear model. This technique enables us to extract brain regions which show correlations between tissue volume and variables, such as age, sex, and other subject's characteristics. We can analyze not only age-related normal changes but also diseased brain, such as dementia and schizophrenia. It has been believed that functional imaging precede structural imaging to detect early pathological findings of the diseases. However, recent development of high-resolution structural imaging and sophisticated analytical technique enable us to detect the brain disease at very early stage. Now we have collected over 3,000 brain MRI of healthy Japanese aged from 5 to 80 and constructed an MRI database together with their characteristics such as age, sex, lifestyle information, blood pressure, present and past disease history, and cognitive functions. This is a largest brain MRI database in Japan and one of the largest one in the world.

20.2 Imaging Studies of Brain Development

20.2.1 Correlation Between Gray Matter Density-Adjusted Brain Perfusion and Age Using Brain MR Images of 202 Healthy Children

In understanding brain aging, the knowledge of brain maturation is very important, for the relationship between brain maturation and brain aging is regarding as a "mirror pattern." In detail, brain regions that mature earlier such as occipital regions are robust in brain aging, whereas brain regions that mature rather late such as prefrontal regions are vulnerable for aging. Brain development continues through childhood and adolescence. Recently, it has been revealed that human brain development is a structurally and functionally nonlinear process. However, despite this growing wealth of knowledge about maturational changes in brain structure in children, the trajectory of brain perfusion with age in healthy children is not yet well documented.

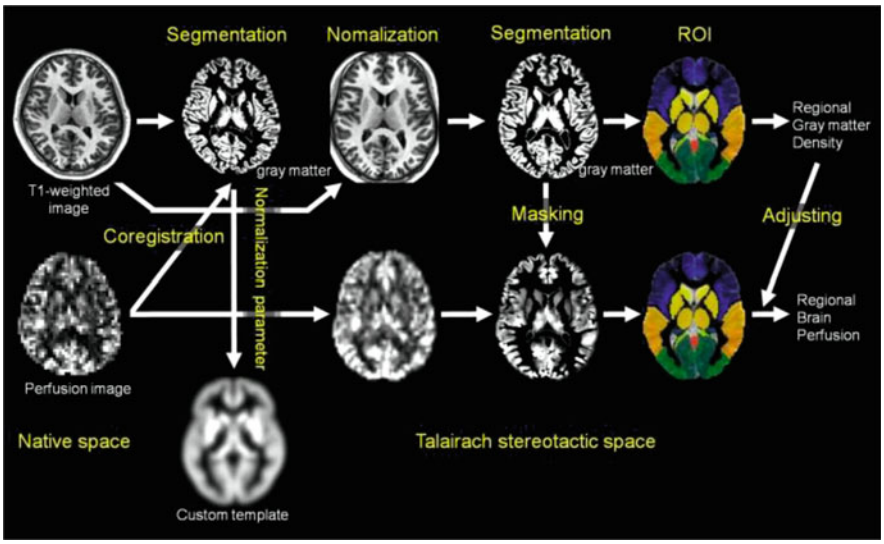

Fig. 20.1 Schematic of the image analysis

Recently, arterial spin-labeling (ASL) perfusion magnetic resonance imaging (MRI) has been developed for evaluating brain perfusion. We examined the correlation between brain perfusion and age using pulsed ASL MRI in a large number of healthy children.

We collected data on brain structural and ASL perfusion MRI in 202 healthy children aged 5–18 years. Structural MRI data were segmented and normalized, applying a voxel-based morphometric analysis. Perfusion MRI was normalized using the normalization parameter of the corresponding structural MRI. We calculated brain perfusion with an adjustment for gray matter density (BP-GMD) by dividing normalized ASL MRI by normalized gray matter segments in 22 regions. Next, we analyzed the correlation between BP-GMD and age in each region by estimating linear, quadratic, and cubic polynomial functions, using the Akaike information criterion (Fig. 20.1).

As a result, the correlation between BP-GMD and age showed an inverted U shape followed by a U-shaped trajectory in most regions [1–3]. In addition, age at which BP-GMD was highest was different among the lobes and gray matter regions, and the BP-GMD association with age increased from the occipital to the frontal lobe via the temporal and parietal lobes.

In the frontal lobe, all gray matter regions showed an inverted U-shaped trajectory for the correlation between BP-GMD and age, and the best fit was a negative quadratic or positive cubic polynomial function. The estimated age at which BP-GMD was highest was earlier in the precentral gyrus, cingulate gyrus, and anterior cingulate cortex than in the superior, middle, and inferior frontal gyri (Fig. 20.2).

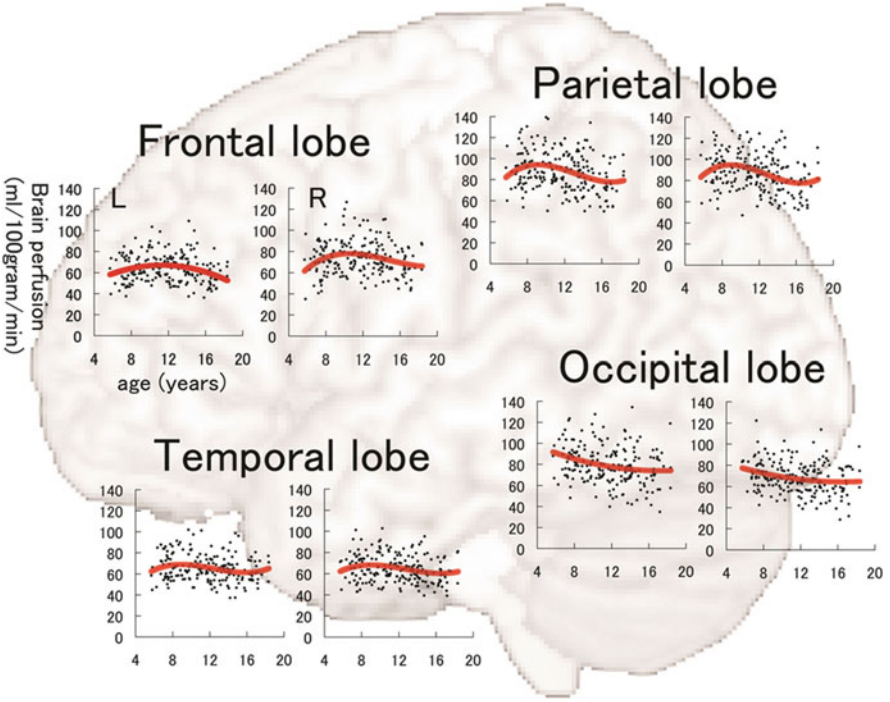

Fig. 20.2 Correlation between brain perfusion, adjusted for gray matter density, and age in the frontal lobe, parietal lobe, occipital lobe, and temporal lobe in each hemisphere

We demonstrated a correlation between BP-GMD and age using ASL brain perfusion MRI in a large number of healthy children over a wide age range. As a result, the trajectory of the correlation between BP-GMD and age showed an inverted U-shaped second-order polynomial function in most regions in the frontal lobe, a third-order polynomial function in the parietal and temporal lobes, and a U-shaped second-order and negative linear correlation in the occipital lobe. Our results indicate that higher-order association cortices mature after the lower-order cortices in terms of brain perfusion. As a result, the trajectory of the correlation between BP-GMD and age showed an inverted U shape followed by a U-shaped trajectory in most regions. In addition, the age at which BP-GMD was highest was different among the lobes and gray matter regions, showing a progression from the occipital lobe to the frontal lobe, via the temporal and parietal lobes. Our results indicate that higher-order association cortices mature after the lower-order cortices mature. This may help not only clarify the mechanisms of normal brain maturation from the viewpoint of brain perfusion but also distinguish normal from developmental disorders that show abnormal brain perfusion patterns.

20.2.2 Correlation Between Sleep Duration and Gray Matter Volume Using Brain MR Images of 290 Healthy Children

Sleep is essential for living beings, and sleep loss has been shown to affect hippocampal structure and function in rats by inhibiting cell proliferation and neurogenesis in this region of the brain. We aimed to analyze the correlation between sleep duration and the hippocampal volume using brain magnetic resonance images of 290 healthy children aged 5–18 years. We examined the volume of gray matter, white matter, and the cerebrospinal fluid (CSF) space in the brain using a fully automated and established neuroimaging technique, voxel-based morphometry, which enabled global analysis of brain structure without bias toward any specific brain region while permitting the identification of potential differences or abnormalities in brain structures. We found that the regional gray matter volume of the bilateral hippocampal body was significantly positively correlated with sleep duration during weekdays after adjusting for age, sex, and intracranial volume [4]. Our results indicated that sleep duration affects the hippocampal regional gray matter volume of healthy children. These findings advance our understanding of the importance of sleep habits in the daily lives of healthy children.

20.3 Imaging Studies of Brain Aging

20.3.1 Correlation Between Baseline Regional Gray Matter Volume and Global Gray Matter Volume Decline Rate

Evaluating whole-brain or global gray matter volume decline rate is important in distinguishing neurodegenerative diseases from normal aging and in anticipating cognitive decline over a given period in non-demented subjects. Whether a significant negative correlation exists between baseline regional gray matter volume of several regions and global gray matter volume decline in the subsequent time period in healthy subjects has not yet been clarified. Therefore, we analyzed the correlation between baseline regional gray matter volumes and the rate of global gray matter volume decline in the period following baseline using magnetic resonance images of the brains of 381 healthy subjects by applying a longitudinal design over 6 years using voxel-based morphometry.

All subjects were Japanese individuals recruited from our previous brain-imaging project. We selected participants who had lived in Sendai City at the time of the previous study, whose collected data had no missing values and who had no serious medical problems from an initial 1604 eligible persons. All participants were screened with a mail-in health questionnaire and underwent telephone and personal interviews. Persons who reported a history of any malignant tumor,

head trauma with loss of consciousness for >5 min, cerebrovascular disease, epilepsy, any psychiatric disease, or claustrophobia were excluded from the study. All subjects were screened for dementia using the Mini-Mental State Examination (MMSE). An experienced neuroradiologist examined the MR scans for any tumors and cerebrovascular disease. The final sample consisted of 381 participants (40.1 % of the eligible cohort: 158 men, 223 women). All images were collected using the same 0.5 T MR scanner, including baseline images using MP-RAGE pulse sequences. After the image acquisition, all MR images were analyzed using statistical parametric mapping 2 in Matlab. We calculated gray matter volume and white matter volume using fully automated techniques. To normalize the head size of each subject, we defined the gray matter ratio (GMR) as the percentage of gray matter volume divided by the intracranial volume. Next, to reveal the annualized rate of change in GMR with age, we determined the annual percentage change in GMR (APC_{GMR}) for each subject. We determined regional gray matter volume using voxel-based morphometry. To investigate the correlation between baseline regional gray matter volume and APC_{GMR}, we performed a multiple regression analysis with age, gender, intracranial volume, and APC_{GMR} as independent valuables and baseline regional gray matter volume as a dependent valuable. We used the random field theory method to correct for the Familywise Error Rate (FWE); any resulting *P*-value less than 0.05 was considered significant. Next, we tested whether the gray matter regional volume that showed the significant negative correlation with APC_{GMR} at baseline could predict whether the APC_{GMR} was above or below the APC_{GMR} mean by applying a standard (not stepwise) linear discriminant analysis in SPSS11.5. For the discriminant analysis, we used the mean gray matter volume over a cluster in each region, and the regional gray matter volume as defined by multiple regression analysis. We set the significance level at $P < 0.05$.

As a result, the gray matter regions showing significant negative correlation with APC_{GMR} adjusted for age, gender, and intracranial volume are shown in Fig. 20.1. Baseline regional gray matter volumes of the right PCC/precuneus and the left hippocampus showed significant negative correlations with APC_{GMR} after adjusting for age, gender, and intracranial volume (right PCC/precuneus, $t = 5.42$, $P = 0.020$; left hippocampus, $t = 5.29$, $P = 0.035$) [1]. Therefore, we used the gray matter regions of the right PCC/precuneus and the left hippocampus in the next discriminant analysis. Baseline regional gray matter volume of both the right PCC/precuneus and the left hippocampus significantly distinguished whether APC_{GMR} was above or below the APC_{GMR} mean. The F-value, *p*-value, and discriminant function coefficient were 13.51, <0.001, and 0.833 in the right PCC/precuneus and 5.71, 0.017, and 0.350 in the left hippocampus, respectively. Overall, 58.4 % of the APC_{GMR} (55.8 % of APC_{GMR} below the mean of APC_{GMR} and 60.9 % of APC_{GMR} above the mean of APC_{GMR}) was correctly distinguished using the discriminant function (Fig. 20.3).

This study provides the first longitudinal findings showing that baseline regional gray matter volumes in the right PCC/precuneus and the left hippocampus show a significant negative correlation with the rate of global gray matter volume decline

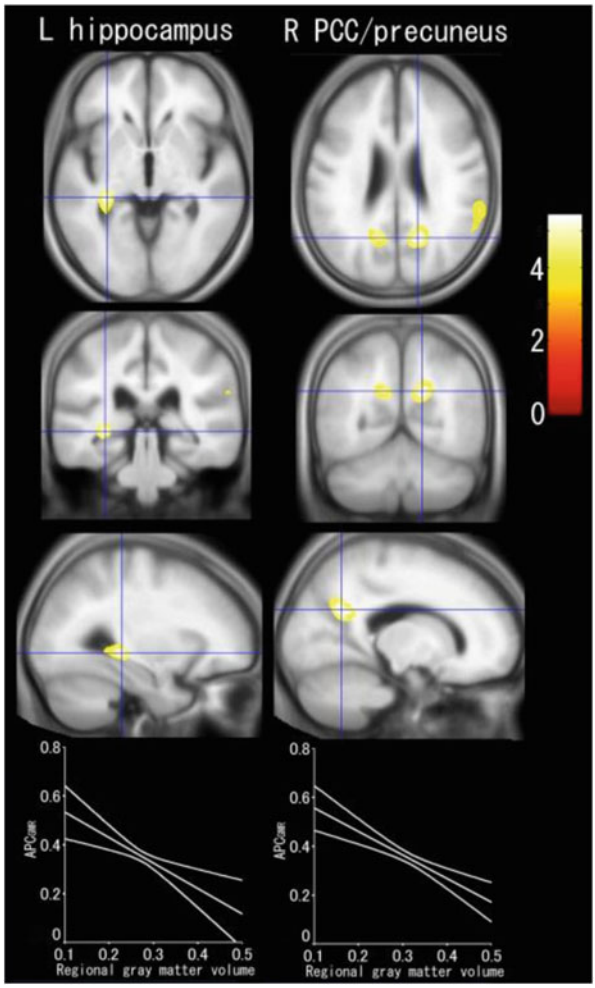

Fig. 20.3 Gray matter regions showing significant negative correlations with annual percent change of the gray matter ratio (APC_{GMR}) adjusted for age, gender, and intracranial volume

in the following period, as represented by APC_{GMR}, adjusting for age, gender, and intracranial volume. In addition, baseline regional gray matter volumes of both the right PCC/precuneus and the left hippocampus significantly distinguished whether the APC_{GMR} was above or below the APC_{GMR} mean. These results indicate that subjects who had smaller baseline regional gray matter volumes in those regions showed higher rate of global gray matter volume decline in the following period.

In summary, using a longitudinal design over 6 years in 381 community-dwelling healthy individuals, we examined the correlation between baseline regional gray matter volume and the rate of global gray matter volume decline in the following period. We found a significant negative correlation between APC_{GMR} and the baseline regional gray matter volumes of the right PCC/precunei and the left hippocampus after adjusting for age and gender. In addition, baseline regional gray

matter volume of both the right PCC/precuneus and the left hippocampus significantly distinguished whether the APC_{GMR} was above or below the APC_{GMR} mean. Our results suggest that baseline regional gray matter volume predicts the rate of global gray matter volume decline in the following period in healthy subjects. Our study may contribute to distinguishing neurodegenerative diseases from normal aging and to predicting cognitive decline.

20.3.2 Correlation Between Degree of White Matter Hyperintensities and Global Gray Matter Volume Decline Rate

Whether the degree of white matter hyperintensities (WMHs) shows a significant correlation with the rate of global gray matter volume decline over a period following initial baseline measurement remains unclear. The purpose of the present study was to reveal the relationship between the degree of WMHs at baseline and the rate of global gray matter volume decline by applying a longitudinal design. Using a 6-year longitudinal design and magnetic resonance images of the brains of 160 healthy individuals aged over 50 years and living in the community, we analyzed the correlation between degree of WMHs using Fazekas scaling at baseline and rate of global gray matter volume decline 6 years later. To obtain the rate of global gray matter volume decline, we calculated global gray matter volume and intracranial volume at baseline and at follow-up using a fully automated method. As a result, the annual percentage change in the gray matter ratio (GMR, APC_{GMR}), in which GMR represents the percentage of gray matter volume in the intracranial volume, showed a significant positive correlation with the degree of deep WMHs and periventricular WMHs at baseline, after adjusting for age, gender, present history of hypertension, and diabetes mellitus [2].

The degree of WMHs, both DWMH and PVWMH, at baseline showed a significant positive correlation with the rate of global gray matter volume decline, represented by APC_{GMR}, adjusting for age, gender, and present history of hypertension and diabetes mellitus in healthy subjects using longitudinal analysis. To our knowledge, we are the first to show the correlation between the degree of WMHs at baseline and the rate of subsequent global gray matter volume decline in healthy elderly individuals. Our result is partially consistent with recent studies that showed a significant positive correlation between the degree or load of WMHs and decreases in gray matter volume in healthy elderly people, although those studies were conducted using cross-sectional design. However, another recent study using longitudinal analysis has shown that WMH is not a predictor of brain atrophy rate in elderly subjects. The inconsistency between the findings of the recent study and the present study may have arisen from differences in the volume that was measured. In the present study, we focused on the rate of decline of gray matter volume, not whole-brain volume, because gray matter volume is significantly correlated with

several cognitive functions. Our results suggest that the rate of global gray matter volume decline could be predicted using the degree of WMHs at baseline, evaluated by simple visual scaling.

In summary, using a longitudinal design over 6 years in 160 community-dwelling healthy individuals, the degree of WMHs was measured at baseline, and the rate of global gray matter volume decline was obtained. As a result, APC_{GMR} showed a significant positive correlation with the degree of deep WMHs and periventricular WMHs at baseline adjusting for age, gender, and present history of hypertension and diabetes mellitus. Our results suggest that degree of WMHs at baseline predicts the rate of subsequent gray matter volume decline and also suggests that simple visual scaling of WMHs could contribute to the prediction of the rate of global gray matter volume decline.

20.3.3 Risk Factors for Brain Volume Decrease

20.3.3.1 Alcohol Drinking

We also tested the correlation between gray matter ratio and lifetime alcohol intake. There was a strong negative correlation between the log-transformed lifetime alcohol intake and the gray matter ratio [5]. Figure 20.4 shows the gray matter regions that had a significant negative correlation between the lifetime alcohol intake and the regional gray matter volume. The gray matter volume of the bilateral middle frontal gyri showed a significant negative correlation with the log-transformed lifetime alcohol intake.

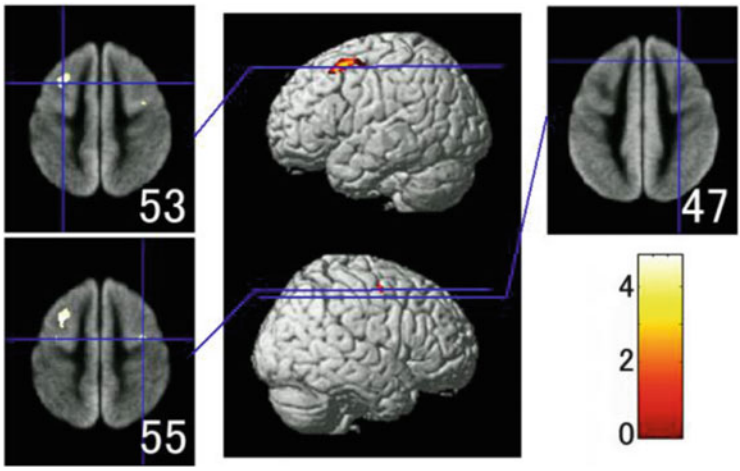

Fig. 20.4 Brain regions that showed negative correction between gray matter volume and lifetime alcohol intake

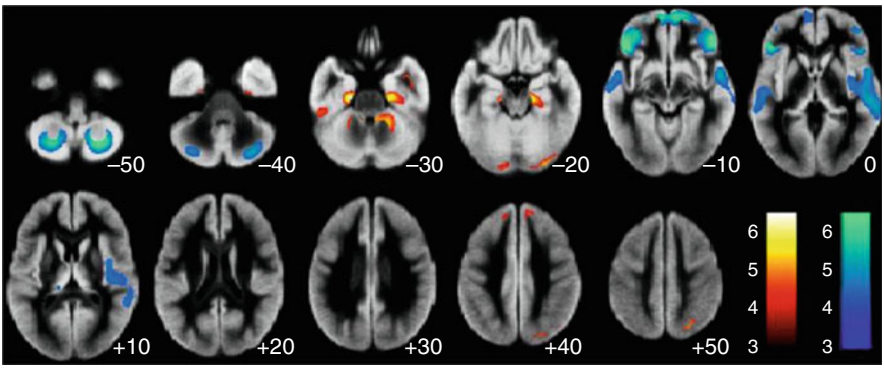

Fig. 20.5 T brain regions that showed correlations between gray matter volume and body mass index (BMI). *Red* and *blue color* indicated negative and positive correlations, respectively

20.3.3.2 Obesity

We tested correlation between gray matter ratio and obesity. As an indicator for obesity, body mass index (BMI) was used. Volumetric analysis revealed that there are significant negative correlations between BMI and the gray matter ratio, which represents the percentage of gray matter volume in the intracranial volume, in men ($p < 0.001$, adjusting for age, systolic blood pressure, and lifetime alcohol intake), whereas not in women. VBM revealed that regional gray matter volumes of the bilateral medial temporal lobe, occipital lobe, frontal lobe, and anterior lobe of the cerebellum show significant negative correlation with BMI, and those of the posterior lobe of the cerebellum, perisylvian regions of the bilateral frontal and temporal lobes, and bilateral orbitofrontal gyri show significant positive correlation with BMI in men [6] (Fig. 20.5).

20.4 Conclusion

We constructed a large-scale brain MRI database for healthy Japanese and clarified age-related volume changes of the human brain and their risk factors. Several factors such as hypertension, alcohol drinking, and obesity are related with gray matter volume reduction of several regions. In addition, we have shown that several factors such as baseline gray matter volume structure and white matter lesions predict the global gray matter volume decline rate. These results may contribute to the understanding of normal brain aging, as well as age-related brain diseases, such as dementia.

References

1. Taki Y, Hashizume H, Sassa Y, Takeuchi H, Wu K, Asano M, Asano K, Fukuda H, Kawashima R. Correlation between gray matter density-adjusted brain perfusion and age using brain MR images of 202 healthy children. Hum Brain Mapp. 2011;32:1973–85.
2. Taki Y, Kinomura S, Sato K, Goto R, Wu K, Kawashima R, Fukuda H. Correlation between baseline regional gray matter volume and global gray matter volume decline rate. Neuroimage. 2011;54:743–9.
3. Taki Y, Kinomura S, Sato K, Goto R, Wu K, Kawashima R, Fukuda H. Correlation between degree of white matter hyperintensities and global gray matter volume decline rate. Neuroradiology. 2011;53:397–403.
4. Taki Y, Thyreau B, Hashizume H, Sassa Y, Takeuchi H, Wu K, Kotozaki Y, Nouchi R, Asano M, Asano K, Fukuda H, Kawashima R. Sleep duration during weekdays affects hippocampal gray matter volume in healthy children. NeuroImage. 2012;60:471–5.
5. Taki Y, Kinomura S, Sato K, Goto R, Inoue K, Okada K, Ono S, Kawashima R, Fukuda H. Both global gray matter volume and regional gray matter volume negatively correlate with lifetime alcohol intake in non-alcohol-dependent Japanese men. A volumetric analysis and a voxel-based morphometry. Alcoholism Clin Exp Res. 2006;30:1045–50.
6. Taki Y, Kinomura S, Sato K, Inoue K, Goto R, Okada K, Uchida S, Kawashima R, Fukuda H. Relationship between body mass index and gray matter volumes in 1428 healthy individuals. Obes Res. 2008;16:119–24.